ALMA MATER STUDIORUM · UNIVERSITÀ DI BOLOGNA

Scuola di Scienze

Corso di Laurea Magistrale in Fisica

In-situ detection of defect formation in organic flexible electronics by Kelvin Probe Force Microscopy

Relatore:
Prof.ssa Beatrice Fraboni

Correlatore:
Dott. Tobias Cramer

Presentata da:
Lorenzo Travaglini

Sessione III
Anno Accademico 2014/2015

Abstract

Organic semiconductor technology has attracted considerable research interest in view of its great promise for large area, lightweight, and flexible electronics applications. Owing to their advantages in processing and unique physical (i.e., electrical, optical, thermal, and magnetic) properties, organic semiconductors can bring exciting new opportunities for broad-impact applications requiring large area coverage, mechanical flexibility, low-temperature processing, and low cost. Thus, organic semiconductors have appeal for a board range of devices including transistors, diodes, sensor, solar cells, and light-emitting devices. In order to improve the resistance of organic electronics to mechanical strain and to achieve highly flexible device architecture it is crucial to understand on a microscopic scale how mechanical deformation affects the electrical performance of organic thin film devices. Towards this aim, I established in this thesis the experimental technique of Kelvin Probe Force Microscopy (KPFM) as a tool to investigate the morphology and the surface potential of organic semiconducting thin films under mechanical strain.

KPFM has been employed to investigate the strain response of two different organic thin film transistors with organic semiconductor made by 6,13-bis(triisopropylsilylethynyl)-pentacene (TIPS-Pentacene), and Poly(3-hexylthiophene-2,5-diyl) (P3HT) respectively. The results show that this technique allows to investigate on a microscopic scale failure of flexible thin film transistors with this kind of materials during bending. I find that the abrupt reduction of TIPS-pentacene device performance at critical bending radii is related to the formation of nano-cracks in the microcrystal morphology. The cracks are easily identified due to the abrupt variation in surface potential caused by local increase in resistance. Numerical simulation of the bending mechanics of the hole transistor structure further identifies the mechanical strain exerted on the TIPS-pentacene micro-crystals as the fundamental origin of fracture.

Instead for P3HT based transistors no significant reduction in electrical performance is observed during bending. This finding is attributed to the amorphous nature of the polymer giving rise to an elastic response without the occurrence of crack formation.

Abstract

La tecnologia basata sui semiconduttori organici ha suscitato un notevole interesse nell'ambito della ricerca in vista delle sue promettenti applicazioni nell'elettronica flessibile quali ricoprire vaste aree, leggerezza e flessibilità. A causa dei loro vantaggi operativi e proprietà fisiche uniche (elettriche, ottiche, termiche e magnetiche), i semiconduttori organici possono portare nuove opportunità per le applicazioni ad ampio impatto che richiedono ampia area di copertura, lavorazione a bassa temperatura e basso costo. Così, i semiconduttori organici hanno applicazione in una vasta gamma di dispositivi tra cui transistor, diodi, sensori, celle solari, e dispositivi emettitori di luce. Per migliorare la resistenza dell'elettronica organica a sollecitazioni meccaniche e per realizzare architetture dei dispositivi altamente flessibili è fondamentale comprendere in scala microscopica come la deformazione meccanica influisce sulle prestazioni elettriche dei dispositivi organici a film sottile. A tale scopo, ho stabilito in questa tesi la tecnica sperimentale Kelvin Probe Force Microscopy (KPFM) come uno strumento per indagare la morfologia e il potenziale di superficie dei semiconduttori organici a film sottile sotto sollecitazioni meccaniche.

La tecnica KPFM è stata impiegata per studiare la risposta alle sollecitazioni meccaniche di due differenti transistor a film sottile con la regione attiva costituita da 6,13-bis(triisopropylsilylethynyl)-pentacene (TIPS-Pentacene), e Poly(3-hexylthiophene-2,5-diyl) (P3HT) rispettivamente. I risultati mostrano che questa tecnica è utile ad indagare in scala microscopica problematiche dei transistor a film sottile flessibili, con questo tipo di materiali, durante la piegatura.

Ho trovato che la brusca riduzione delle prestazioni del dispositivo con TIPS-Pentacene a certi raggi di curvatura è legata alla formazione di nano-cracks nella morfologia dei micro cristalli per il caso del film costituito da TIPS-Pentacene. I crack sono facilmente identificabili a causa della brusca variazione del potenziale di superficie causata da un aumento locale della resistenza.

Simulazione numerica della meccanica del piegamento della struttura del transistor identifica ulteriormente le sollecitazioni meccaniche sui micro cristalli di TIPS-Pentacene come origine fondamentale della frattura.

Per il caso dei transistor basati sul P3HT non si nota una significativa riduzione delle prestazioni del dispositivo durante il piegamento. Questa osservazione è attribuita alla natura amorfa del polimeriche da luogo ad una risposta elastica senza il verificarsi di una formazione di crepe.

Contents

Introduction

With the invention of the transistor around the middle of the last century, inorganic semiconductors such as Si or Ge began to take over the role as the dominant material in electronics from the previously dominant metals. At the same time, the replacement of vacuum tube based electronics by solid state devices initiated a development, which by the end of the 20th century has led to the omnipresence of semiconductor microelectronics in our everyday life. Now at the beginning of the 21st century we are facing a new electronics revolution that has become possible due to the development and understanding of a new class of materials, commonly known as *organic semiconductors*.

The transistor is a fundamental building block for all modern electronics; transistors based on organic semiconductors as the active layer are referred to as organic thin film transistors (OTFTs). A number of commercial opportunities have been identified for OTFTs, including flat panel active-matrix liquid crystal displays (LCDs) or active matrix organic light-emitting diodes displays (AMOLEDs), electronic paper (e-paper), low-end data storage such as smart cards, radio-frequency identification (RFID) and tracking device, low-cost disposable electronic products, and sensor arrays; more application continue to evolve as the technology matures.

The unique features, which give organic electronics a technological edge, are simpler fabrication methods and the ability to withstand mechanical forces related to flexing or stretching. Fabrication of organic electronics can be done using relatively simple processes such as evaporation, spin-coating, and printing, which do not require high-end clean room laboratories.

Flexibility, or, in other words, the possibility of adapting the fabricated devices on different kinds of substrates, is certainly one of the main advantages of this new technology. For this reason, many efforts have been recently made to develop flexible OTFT systems for applications in which devices are continuously exposed to mechanical stress, such as, for instance, in wearable electronics. As a matter of fact, organic semiconductor based device are severely affected by mechanical deformation. In particular, the surface strain induced on the active layer usually gives rise to pronounced variations in the conductivity of the device.

This feature in some cases was used for the fabrication of OFET-based mechanical sensors; on the other hand, there are many applications in which this mechanical sensitivity is undesired, because device are required to operate normally even during mechanical deformation. Therefore, investigating the mechanical properties of organic semiconductor is of a crucial importance for addressing the different requirements of these applications.

In order to shed some light on the mechanical sensitivity of OFETs, many efforts have been aimed towards the investigation of the main causes that lead organic semiconductors to be sensitive to mechanical stress [1][2][3]. In many cases, the current variation can be correlated to morphological changes taking place in the active layer, thus modifying the hopping energy barrier for charge transport [1][2].Very recently, a correlation was observed between the device electrical behaviour and the modification of the structural properties of the structural properties of the organic active film induced by the mechanical deformation. Moreover it was recently demonstrated by comparing OTFTs realized using two different classes of organic semiconductors, that the intrinsic morphological properties of the organic semiconductor film can dramatically influence the sensitivity of mechanical deformation of the devices.

In this thesis I investigated the microscopic details of these aspects on OFETs with two different types of material for the active region, in particular with TIPS Pentacene and P3HT. I established KPFM as a tool to study morphology, surface potential during mechanical strain. These microscopic investigations were combined with the electrical characterizations of the macroscopic devices with the aim of revealing a possible correlation between morphological properties and device sensitivity to mechanical deformation.

The first chapter of this thesis illustrates the general properties of organic materials and discussing the charge transport mechanism of organic semiconductors.

The second chapter contains an introduction to atomic force microscopy with special emphasis on the non-contact interaction regime and Kelvin Probe Force Microscopy described.

The third chapter describes the general procedures adopted throughout the experimental work, including the description of the typical TFT structure used, the sample preparation, the measurement setup and other methods. The fourth chapter reports the characterization results of the related sample and a discussion of the findings and further implications.

Finally, conclusions are derived in the last chapter.

1 Flexible Organic Electronics

In this chapter, the fundamental properties of organic materials is introduced in section 1.1. Among the organic materials, organic semiconductors are the basis of organic electronics and their most important properties will be treated in subsection 1.2, and the charge transport mechanism of these materials will be illustrated. Section 1.3 and 1.4 describes the electrical characteristics of organic thin film transistors (OTFT) used in these experimental work. In section 1.5 and 1.6 a brief description of the materials used as the active layer of devices [4]-[5].

1.1 Introduction to organic materials

The term “organic semiconductors” is not new. First studies of the photoconductivity of anthracene crystals (prototype of organic semiconductors) were undertaken in early 20st century. The discovery of electroluminescence in the 1960s gave an incentive to study thoroughly the properties of molecular crystals. These studies, however, have only contributed to a better understanding of the theoretical basis of optical excitation and electric charge transfer in organic materials, rather than solve the problems that precluded the use thereof on an industrial scale (low stability, low electric and luminous efficiency). It was only the successful synthesis and controlled polymer doping, for which the Nobel Prize in chemistry was awarded in 2000, that opened up new area of application for organic conducting materials [6].

The adjective organic used in the expression organic electronics refers to the fact that, in this branch of electronics, the active materials used for the fabrication of devices is organic compounds. Although the distinction between ’organic’ and ’inorganic’ compounds is not always straightforward, an organic molecule is usually defined as a chemical compound containing carbon [7]. For historical reasons, this definition does not include a few types of carbon-containing compounds (such as carbonates, simple oxides of carbon and cyanides, as well as the allotropes of carbon such as diamond and graphite), which are therefore considered inorganic. Consequently, in order to explain and understand the electrical properties of organic compounds it is necessary to describe the electronic configuration of the carbon atom and the way it forms chemical bonds with other atoms (of the same type or belonging to different chemical species). Carbon is an element belonging to the Group 14 of the periodic table. The members of this group are characterised by the fact that they have four electrons in the outer energy level.

There are three naturally occurring isotopes of carbon: carbon-12, carbon-13 and carbon-14 (the number following the element name indicates the total number of neutrons and protons contained into the atom nucleus). Carbon-12 (whose nucleus is formed by six neutrons and six protons) is the most stable of all three isotopes and is also the most abundant, accounting for the 98.89 % of carbon. In this thesis, whenever the name "carbon" is used, the isotope carbon-12 will always be implicitly referred to.

In order to understand the electronic properties of organic compounds it is essential to describe the way carbon electrons are distributed in space and the way they are bonded to the nuclei [8]. In other words, it is necessary to introduce the concepts of atomic orbital and orbital hybridisation. According to quantum mechanics [9], the wave-like behaviour of an electron may be described by a complex wave function depending on both position and time $\Psi(r, t)$; the square modulus $|\Psi|^2$ is equal to a probability density: the integral of the square modulus over a certain volume V gives the probability of finding, at a certain instant t, the electron in that volume.

Let us consider now the following equation:

$$\int_{\Omega} |\Psi(r,t)|^2 dxdydz \geq 0.9 \qquad \textbf{(1.1)}$$

Equation (1.1) defines a volume Ω in which the probability to find an electron (described by $\Psi(r, t)$) is at least the 90%; such a region in space is called atomic orbital and its shape depends on how Ψ is mathematically defined.

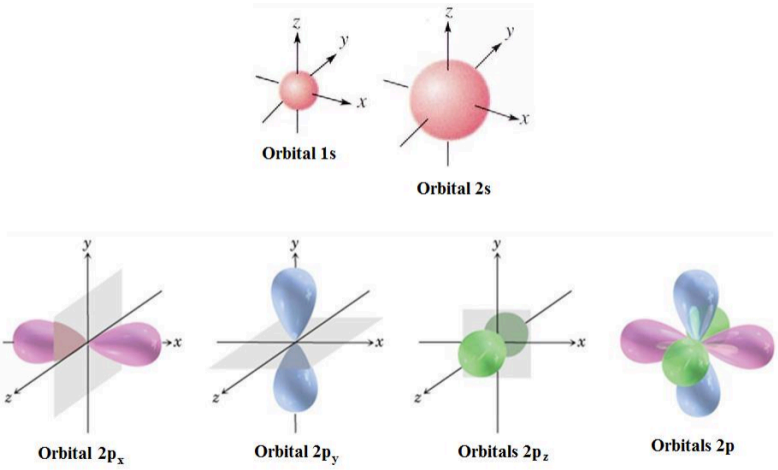

Figure 1.1: shape of the first five orbitals

Each orbital is defined by a different set of quantum numbers and contains a maximum of two electrons. The shape of each orbital depends on the mathematical definition of the wavefunction and

therefore on the value assumed by the *l* quantum number. In Figure 1.1 illustrates the shape of the first five orbitals:

The first two orbitals on top of Figure 1.1 are respectively the orbitals 1s and 2s; they are shaped as spheres centred in correspondence with the atom nucleus. The three orbitals on the bottom are the 2p orbitals; each one of them is shaped as a couple of ellipsoids with a point of tangency in correspondence with the atom nucleus. The three p orbitals are reciprocally orthogonal: if we consider a cartesian coordinate system centred in the nucleus, these orbitals appear aligned along the three axes and are therefore called 2_{px}, 2_{py} and 2_{pz} orbitals.

As mentioned previously, carbon belongs to the Group 14 of the periodic table. It is actually the simplest element of its group, having just six electrons: two of them are contained into the 1s orbital, while the other four are hosted by the second electron shell. When carbon is in its ground state (that is lowest energy state) two of the outer electrons are placed into the 2s orbital while the two remaining electrons are located in two of the 2p orbitals (let us assume, for instance, in 2px and 2py). According to the standard rules set by IUPAC [19], the ground-state electron configuration of carbon may be expressed by the following notation: $1s^2 2s^2 2p_x^1 2p_y^2$ or, in a more compact fashion, $1s^2\ 2s^2\ 2p^2$ [5].

Chemical elements interact with one another through the formation of chemical bonds. From the point of view of organic chemistry, the most important chemical bond is the covalent bond. A covalent bond occurs when two atoms share a pair of electrons; this bond forms when the bonded atoms have a lower total energy than that of widely separated atoms. The formation of a covalent bond requires the partial overlap of two atomic orbitals; the shared electrons have a higher probability to be located in the area between the two atoms nuclei, where the overlap is maximum.

In certain cases, however, the structure of a molecule may not be explained if one considers the orbital shapes previously described. Let us examine, for instance, the simplest organic molecule, namely methane, CH_4 (Figure 1.2)

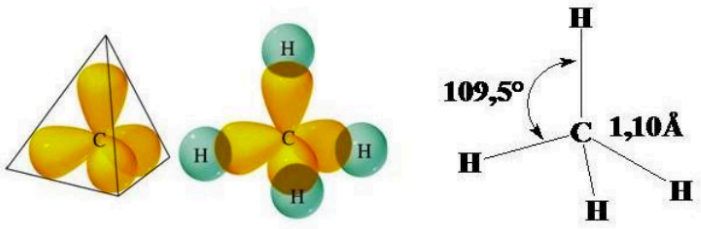

Figure 1.2: Scheme of methane molecule CH_4.

As can be seen from Figure 1.2, methane is characterised by a tetrahedral geometry, in which the carbon atom occupies the tetrahedron centre while the four hydrogen atoms are placed in correspondence with the four-tetrahedron corners. This geometry is not compatible with the orbitals depicted previously; in particular, the three 2p orbitals cannot be geometrically arranged to fit a tetrahedral structure. Linus Pauling solved this problem in 1931, in a famous paper [10] in which the

theory of *orbital hybridisation* was described for the first time. The concept of orbital hybridisation can be explained as follows. Let us take n different orbitals, each one described by its own wavefunction $\Psi_i(r, t)$; when hybridisation occurs, these orbitals are linearly combined in order to form n new hybridised orbitals, each one corresponding to its own wavefunction $\Phi_j(r, t)$ as shown in the following formula:

$$\Phi_j(r,t) = \sum_{i=1}^{n} c_{ij}\Psi_i(r,t) \qquad (1.2)$$

Where coefficients c_{ij} are usually determined to ensure that the wavefunctions describing the hybridised orbitals must be normalised (the integral over all space of their square modulus must be equal to 1), and to guarantee all hybridised orbitals must have the same energy.

From a qualitative point of view, hybridisation may be thought of as a "mix" of an atom orbitals which results in the formation of new, isoenergetic orbitals more suitable for the description of a specific molecule structure.

That being said, the particular structure of methane may be explained if one considers the hybridisation of carbon outer orbitals (namely, 2s and the three 2p orbitals) which results in the formation of four sp^3 orbitals, as shown in Figure 1.3: the four sp^3 orbitals of carbon partially overlap with the 1s orbitals of hydrogen atoms, giving rise to four covalent bonds which are usually indicated as σ-bonds. Other organic molecules show geometrical characteristics which can be explained only considering other forms of hybridisation.

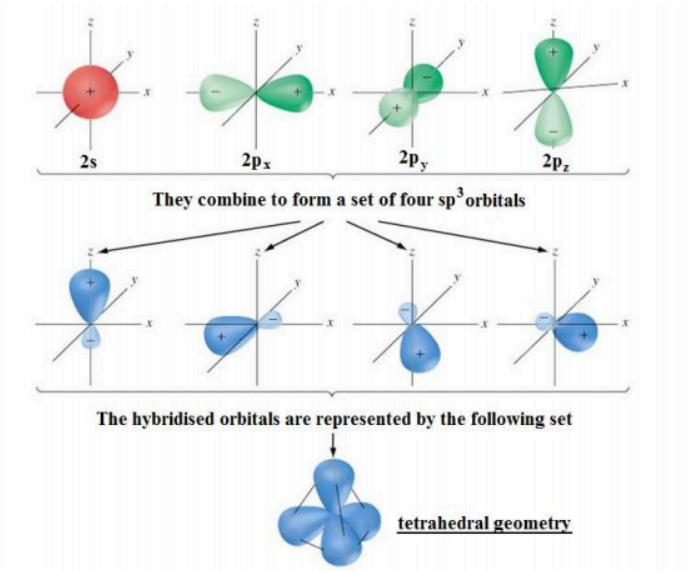

Figure 1.3: Sp^3 hybridisation scheme.

The hybridization sp^2 takes place, for instance, in the ethylene molecule $CH_2{=}CH_2$ (Figure 1.4): Ethylene is a planar molecule whose structure cannot be explained if one considers the original set of carbon orbitals or an sp^3 hybridisation. Indeed, the carbon atoms of ethylene (as well as of all other

compounds where a double C=C bond is present) are characterised by another form of orbital hybridisation, called sp^2 hybridisation where, the 2s orbital and two 2p orbitals (let us assume 2px and 2py) hybridise and form a set of three sp^2 orbitals which lie on the XY plane and are located in correspondence with the corners of an equilateral triangle (Figure 1.5).

The fourth, unhybridised $2p_z$ orbital lies along a direction which is perpendicular to the plane containing the hybridised sp^2 orbitals.

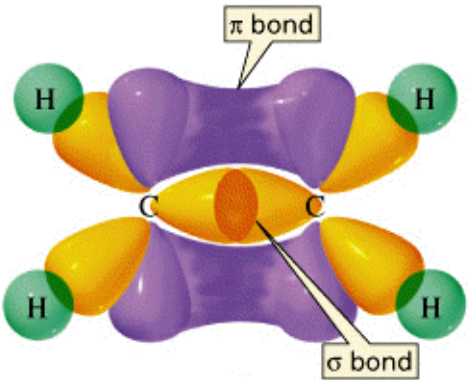

Figure 1.4: Ethylene molecule.

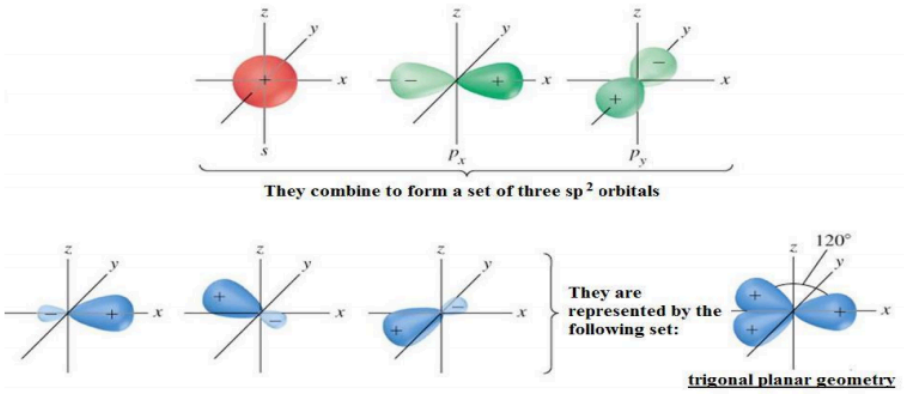

Figure 1.5: Sp^2 hybridization

When two sp^2-hybridised carbon atoms come into close contact in order to form a chemical bond, the orbitals overlap occurs at two different levels. On one hand, one can notice the formation of a covalent σ -bond resulting from the intersection between two sp^2 orbitals along the line joining the two carbon atoms' nuclei. The other two sp^2 orbitals overlap with the hydrogen atoms' 1s orbitals and form two other covalent σ -bonds. When the two carbon atoms come into contact, a partial overlap between the two unhybridized $2p_z$ orbitals occurs.

This overlap is responsible for the formation of a second covalent bond between the carbon atoms, called π bond. These two types of covalent bond are shown in the following picture (Figure 1.6).

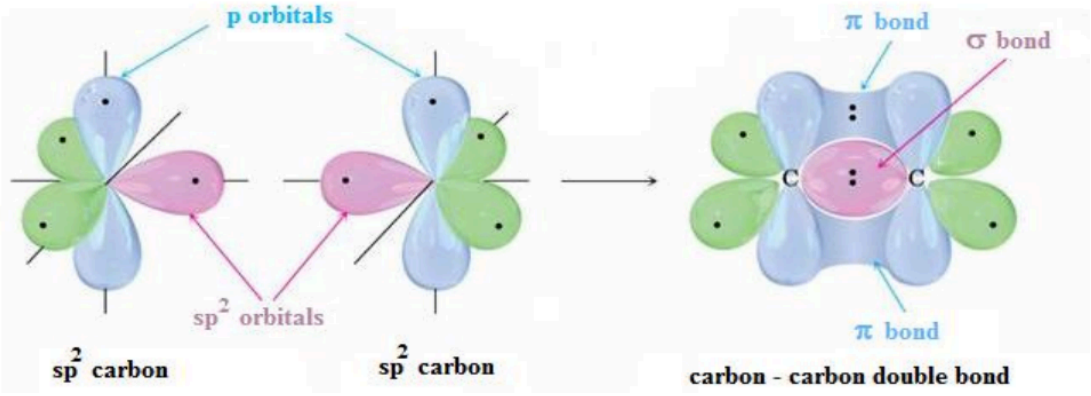

Figure 1.6: formation of carbon-carbon double bound π and σ.

It should be noted that π bonds are less energetic than σ bonds (about 65 kcal/mol versus 80 kcal/mol)[1]. This is essentially due to the fact that, geometrically speaking, a σ bond is characterised by a much larger overlap volume, which causes a stronger constructive interference between the orbitals responsible for the formation of the bond. This phenomenon has very important consequences for the electrical behaviour of the molecule: while σ electrons are strictly confined into the small volume between the two carbon atoms' nuclei, π electrons are able to move into a larger volume and their interaction with the nuclei is relatively weak[1].

1.2 Organic semiconductors

Carbon is a chemical element showing an ability which is almost unique: the capability to form covalent bonds with other carbon atoms and create macromolecules represented by very long chains or more complex structures such as nets. This property is called catenation. Since many organic compounds used in organic electronics are polymers, which are macromolecules obtained through this catenation process, in order to understand the behaviour of organic electronic devices it is necessary to define exactly what polymers are and examine shortly their properties.

According to the definition provided by IUPAC, a polymer may be defined as a molecule of high relative molecular mass, composed of repeating structural units called monomers, characterised by a low relative molecular mass and are interconnected typically by means of covalent bonds.

[1] Carbon also shows a third type or orbital hybridisation called sp hybridisation which leads to the formation of carbon-carbon triple bonds (one σ bond together with two π bonds). From our point of view, this hybridisation is not particularly relevant and therefore will not be described or mentioned in the rest of the thesis.

It is not at all easy to provide general guidelines for the characterisation of a polymer, considering the enormous number of chemical compounds that have been synthesised. However, some classification parameters do exist:

- the chemical characteristics of the composing monomer(s);
- the morphology of the single polymer molecule, that is the geometrical structure formed by the monomers connection (for instance, linear versus branched chain);
- the average molecular weight of a single polymer molecule;
- tacticity (the spatial orientation of the chain's side groups);
- the polymer morphology (the way polymer molecules are spatially arranged in a film or solid);

This last point is extremely important because many electrical transport properties are strictly connected to the morphological features of the polymeric layer. The crystallinity of a polymeric solid is in fact a very important parameter because, as will be shown in the following paragraphs, the conduction behaviour of a polymer is strictly connected to its morphology.

Electronics may be defined as that branch of Physics which studies electronic phenomena occurring within closed paths (electric circuits) designed to carry, manipulate or control electron flow for some purpose. In order to understand how organic devices work it is therefore essential to have a clear picture of the conduction mechanisms in organic conductors and semiconductors.

More specifically, conductive polymers are usually defined as organic polymers able to conduct electricity, exhibiting a conductive or a semiconductive behavior. Conductive polymers can be roughly grouped into three different categories:

- conjugated polymers;
- polymers containing aromatic cycles;
- conjugated polymers containing aromatic cycles.

All the molecules belonging to the previous categories have in common the alternation of single and multiple bonds (usually, double bond) in their structure. This is shown for example, in Figure 1.7, for the simplest conjugated molecule, polyacetylene.

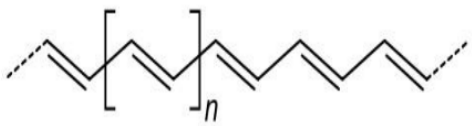

Figure 1.7: Polyacetilene molecule scheme, the simplest example of conjugated molecule.

As can be clearly seen from the picture above, the chain structure of molecules like polyacetylene may be thought of as a sequence of carbon atoms in which sp^3-hybridised carbon atoms are alternated with sp^2-hybridised carbon atoms.

Thanks to this continuous orbital overlap, π electrons (which are loosely bound to the atoms' nuclei) are able to flow along the polymer chain when a voltage is applied to the molecule's extremities, thus enabling the polymer itself to conduct electricity.

A quantitative description of conductivity phenomena in conjugated polymers may be provided through the theory of Molecular Orbitals (MOs). According to this theory, the orbital of a complex molecule (MO) may be expressed starting from the wave functions describing the orbitals of the atoms (AOs) which compose the molecule. From a mathematical point of view, this is usually done by expressing the MO as a linear combination of the AOs; this approach is known through the acronym LCAO (Linear Combination of Atomic Orbitals).

In these molecules, because of this orbitals overlapping, the arrangement of the electrons is reconfigured concerning the energy levels. We can separate the molecular energy levels into two categories: π and π*, bonding and anti-bonding respectively, forming a band-like structure (Figure 1.8). The occupied π-levels are the equivalent of the valence band in inorganic semiconductors.

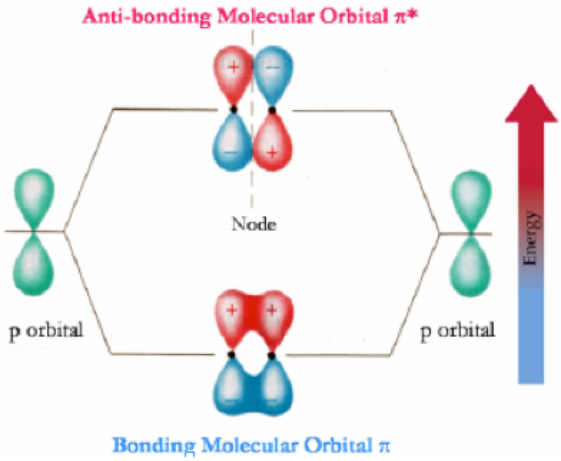

Figure 1.8: The formation of a MO may be graphically described by means of an energy diagram in which the three energy levels (energy of single atoms, energy of bonding MO and energy of anti-bonding MO are reported).

The electrically active level is the highest one and it is called Highest Occupied Molecular Orbital (HOMO). The unoccupied π*-levels are equivalent to the conduction band. In this case, the electrically active level is the lowest one, called Lowest Unoccupied Molecular Orbital (LUMO). The resulting band gap is given by the difference of the energy between HOMO and LUMO.

If we consider a polymer chain with N atoms using the quantum mechanical model for a free electron in a one dimensional box, the wave functions for the electrons of the polymer chain is given by:

$$E_n = \frac{n^2 h^2}{8mL^2}$$

(1.3)

with n=1, 2, 3 etc…and where h is the Plank constant, m the electron mass and L the conjugation length, which, if we consider N atoms separated by a distance d within the polymer chain, is equal to Nd. Therefore, if the π-electrons from the p-orbitals of the N atoms occupy these molecular orbits, with 2 electrons per orbit, then the HOMO should have an energy given by:

$$E\ (HOMO) = \frac{\left(\frac{N}{2}\right)^2 h^2}{8mL^2} \qquad (1.4)$$

whereas, the LUMO will have an energy of:

$$E\ (LUMO) = \frac{\left(\frac{N}{2}+1\right)^2 h^2}{8m(Nd)^2} \qquad (1.5)$$

All energies are supposed to be measured with respect to vacuum energy level as reference. Thus, the energy required to excite an electron from the HOMO to the LUMO is give by their energies difference:

$$E_g = E(LUMO) - E(HOMO) = \frac{(N+1)^2 h^2}{8m(Nd)^2} \cong \frac{h^2}{8md^2N} \quad for\ large\ N \qquad (1.6)$$

It is evident that the band gap is inversely proportional to the conjugation length L, and, as a consequence, to the number of atoms N in the polymer chain. If the band gap is high the material is an insulator, if it is low the material is a conductor. Usually the most of the organic semiconductors have a band gap between 1.5 to 3 eV.

1.3 Charge carrier transport in organic materials

Inorganic semiconductors such as Si or Ge, atoms are held together by very strong covalent bonds and charge carriers moves as highly delocalized plane waves in wide bands and usually have very high mobility.

However, when polymer molecules aggregate, the resulting polymeric solids exhibit different crystallinity degree, varying from almost perfect crystals to amorphous solids [11]. As a consequence,

charge carrier transport in such solids varies in a range delimited by two extreme cases: band transport and hopping.

Band transport is normally observed only in pure, single organic crystals [46]. In such materials, charge mobility depends on temperature according to the following power law:

$$\mu \propto T^{-n} \; with \; n = 1 \dots 3 \qquad (1.7)$$

In highly disordered polymeric solids, such as amorphous solids, transport usually proceeds via hopping and is thermally activated. In amorphous solids, molecules are arranged in a random, disordered way. Therefore, energy states are not organised in continuous bands separated by an energy gap but instead localised energy states (i.e. existing only for discrete values of the wave number k) occur. The density of these states is usually described using a couple of Gaussian distributions, the Gaussian functions being centred in correspondence with the energy level where the majority of levels appear. The functions peaks may be interpreted as analogous to conduction and valence bands in crystalline semiconductors (Figure 1.9).

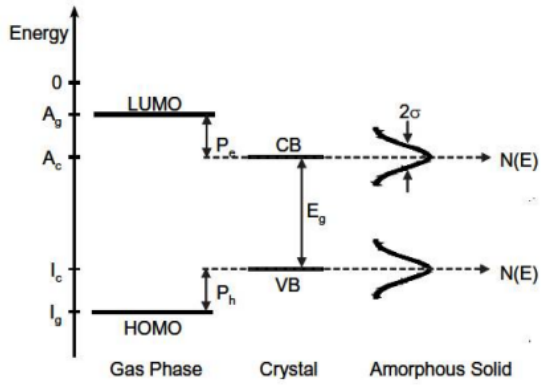

Figure 1.9:Energy diagrams in different types of organic semiconductors.

In amorphous solids, charge flow takes place when electrons start moving (hopping) from lower energy levels to higher energy levels. This flow is due to an increment in electrons energy which may be caused both by temperature or the application of an external electric field. A simple model frequently used in order to express mathematically the mobility dependence on the factors cited above is the following:

$$\mu(F,T) \propto \exp\left(-\frac{\Delta I}{kT}\right) exp\left(\frac{\beta\sqrt{F}}{kT}\right) \qquad (1.8)$$

where ΔE is a parameter called activation energy (i.e. the minimum amount of energy to be provided in order to start conduction) and F represents the applied electric field. The case of semicrystalline polymeric solids is perhaps the most complicated, from an analytical point of view. These solids

usually assume a polycrystalline structure, in other words they may be thought of as many crystalline grains immersed into an amorphous matrix. While within the grains charges move thanks to band transport, the problem arises in correspondence with the grain boundaries. Here, mobile charges are temporarily immobilised (trapping) thus creating a potential barrier which electrostatically repels same sign charges; as a consequence, charge mobility is greatly decreased. A simple expression utilised in order to express mobility in polycrystalline semiconductors is given by the following:

$$\mu \propto \mu_0 exp\left(-\frac{E_b}{kT}\right) \qquad (1.9)$$

In (1.9), μ_0 is the mobility in crystalline grains and E_b is the height of potential barrier.
Even though the MOSFET laws are taken as representative also for OFETs, it is well known that, in most cases, the typical behaviour strongly differs from the ideal case. The main reason for such discrepancy is generally ascribed to the intrinsic structural properties of the organic semiconductors. Usually, when we grow an organic semiconductor film, we do not obtain a crystal structure; a single organic crystal can be obtained only under strict deposition conditions. Therefore, when we talk about organic semiconductors, we suppose to discuss about polycrystalline thin film, with a very hight concentration of structural defects which in the main reason for the non linearity usually observed in such devices. Every defect acts as scattering site for charge carriers, causing the distortion in the, ideally, periodic lattice potential. Therefore, a band-like transport is usually impeded by such scattering process. The effect of defects is even stronger if the defects themselves act as trapping sites for charge carriers. Trapping is relevant when the defect induces one or more energy levels in the band gap of the organic “crystal”. A charge carrier will prefer to occupy this lower energy level and the trap localizes the charge carrier in its site. The presence of traps within the semiconductor layer can cause a decrease in the density of mobile charges, since trapped carriers are localized at the defect sites. In some cases, when the density of defects is high and they strongly localize charge carriers, their influence can completely dominate charge transport across the semiconductor.
Several experiments have been performed on OFETs and several models have been introduced to study charge transport of both polycrystalline and crystalline active layers and its dependence to charge trapping. However, a universal theory which can properly describe charge transport in organic materials does not exist and transport properties are still not fully explained.

1.4 Thin film transistors

The interest for Organic Field Effect Transistors (OFETs) has drastically increased over the past few years, and they have been intensively studied for many application such as displays, smart tags and

sensors. The reason for focused research interest in the field of "plastic electronics" is the opportunity to produce low cost device on plastic substrates on large areas, opening, indeed, an entire market segment. So far, field effect mobilities up to 30 cm^2/Vs have been reported for thin film and single crystal OFETs. However, this value is usually lowered by at least one order of magnitude for organic transistor made on plastic substrates. OFETs are close relatives of the classic Metal Oxide Semiconductor Field Effect Transistors (MOSFETs); typically, since the organic semiconductors are characterized by a low conductivity if compared to inorganic ones, Thin Film Transistor (TFT) architecture is preferred in this case.

The core of an OFET is a Metal-Isulator-Semiconductor structure (MIS), which can in principle be considered as a parallel plate capacitor: the two capacitor plates are formed by a metal electrode, called gate electrode, and a semiconductor, which are separated by a thin insulating film, called gate dielectric (see Figure 1.10). Two additional electrodes, called Source and Drain electrodes are patterned in order to contact the organic semiconductor allowing to probe the conduction across the organic film.

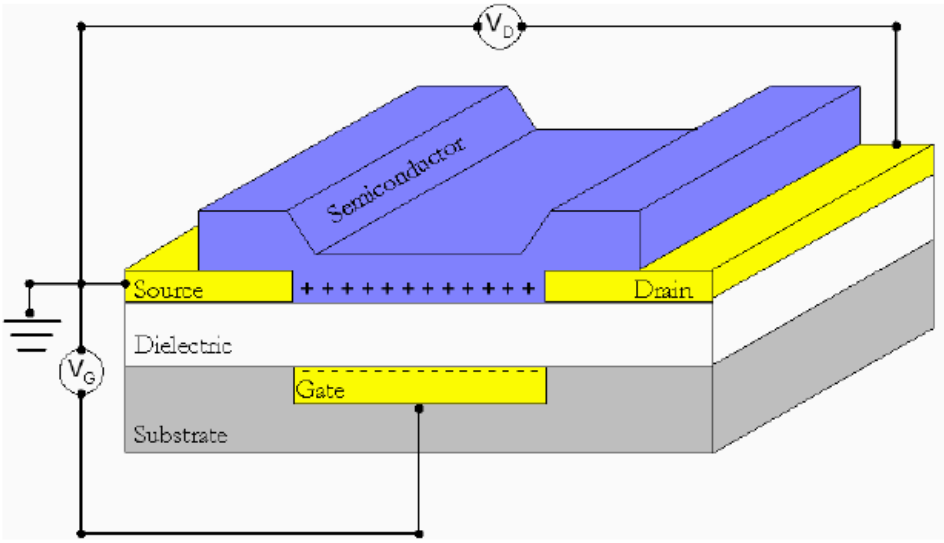

Figure 1.10: Schematic of the OFETs geometry.

One of the main differences between an OFET and the classic MOSFET is that while the latter typically works in inversion mode, OFETs usually work in accumulation mode. When a negative (positive) voltage is applied between the gate and the source electrodes, an electric field is induced in the semiconductor that attracts positive (negative) charge carriers at the semiconductor/insulator interface overlapping with the gate. Applying a negative (positive) voltage between source and drain electrodes, it is possible to drive the positive (negative) charge carriers across the channel area. Charge transport in OFETs is substantially two-dimensional. Charge carrier accumulation is highly localized at the interface between the organic semiconductor and the gate dielectric, and the bulk of the material is hardly or not affected by gate induced field. Upon increasing gate voltage to positive (negative) values, the number of charge carriers accumulated in the channel will reduce until the

channel is fully depleted of free carriers. From this point on, negative (positive) charge are induced in the channel and the device should in principle work in inversion regime. In practise, the flowing current detectable in inversion regime is negligible because the number of charge carriers injected into channel is low due to the high injection barrier at the interface between metal electrodes/semiconductor. The boundary between accumulation and inversion regime is called threshold voltage V_T of the device. Below the threshold voltage the device is in its off state, no free charge carriers are present in the channel and no current flow across it.

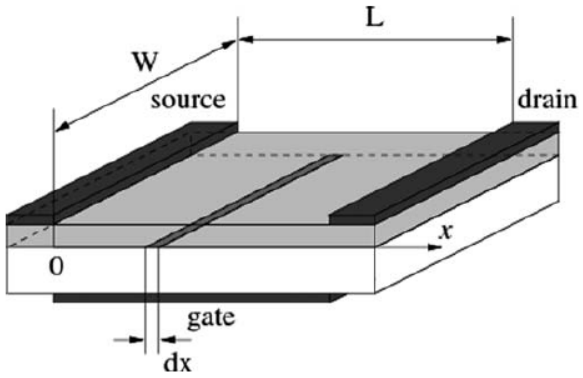

Figure 1.11: Scheme of the TFT with parameters.

The geometric parameters needed to derive an expression for the current in a TFT starting from classical electrodynamics are illustrated in Figure 1.11. The first step is to estimate the charge dq induced by applying a voltage V_G to the gate in an elemental strip of width dx at a distance x from the source. Below threshold, the charge is zero. Above threshold, it becomes

$$dq = -C_i[V_G - V_T - V(x)]Wdx \qquad (1.10)$$

Here, V_T is the threshold voltage and V(x) the potential at the position x of the channel induced by the application of the drain bias; V(x)=0 at the source and V(x)=V_D at the drain. C_i is the capacitance per unit area of the dielectric layer and W the channel width, so that Wdx represents the area of the elemental strip.

The minus sign at the right hand side of equation (1.10) arises from the fact that V_G is applied to the gate (one of the plate of the capacitor), while we are interested in the charge on the other plate (the conducting channel).

The current I_D that flows between source and drain corresponds to the passage of the elemental charge dq during the elemental time dt:

$$I_D = \frac{dq}{dt} = \frac{dq}{dx}\frac{dx}{dt} \tag{1.11}$$

The mobility μ is defined as the ratio between the mean velocity v=dx/dt of the charge carriers and the electric field E= −dV/dx, so that dx/dt=−μ(dV/dx). Making use of equations (1.10) and (1.11) can be rearranged as

$$I_D \mathrm{dx} = W C_i \mu [V_G - V_T - V(x)] dV \tag{1.12}$$

The drain current is now obtained by integrating equation (1.12) from source (x=0, V(x)=0) to drain (x=L, V(x) =V_D). Assuming constant mobility, this leads to

$$I_D = \frac{W}{L} C_i \mu \left[V_G - V_T - \frac{V_D}{2} \right] V_D \tag{1.13}$$

Equation (1.13) corresponds to the so-called linear regime, where $V_D < V_G - V_T$.As V_D increases, the voltage at the drain electrode gradually decreases, up to a point where it falls to zero.
This occurs at the so-called pinch off point, when $V_D = V_G - V_T$. Beyond pinch off, a narrow depletion zone forms next to the drain because the local potential there drops below threshold. Further increase of V_D leads to a slight extension of the depletion zone and a subsequent shift of the pinch off point towards the source. Because the potential at the pinch off point remains equal to $V_G - V_T$, the drain current becomes independent of the drain voltage; this is the saturation regime. Here, the current is obtained by equating V_D to $V_G - V_T$ in equation (1.13):

$$I_D = \frac{W}{2L} C_i \mu [V_G - V_T]^2 \tag{1.14}$$

Because there are two independent voltages, the current–voltage curves of a transistor are of two sorts: in the output characteristic, a set of drain current versus drain voltage curves are drawn for various gate voltages; conversely, transfer characteristics are those in which the drain current is plotted as a function of the gate voltage for a given drain voltage. As will be seen in the following, parameter extraction is carried out from the latter set of curves.

The first examples of OFETs were hybrid structures, where the only "organic" part in the device, was the semiconductor. Typically, the first OFETs were assembled on highly doped silicon wafer, acting at the same time as substrate and as gate electrode. A thin SiO_2 layer was employed as gate dielectric, whereas metals (i.e. Au, Al) were used for the fabrication of the source and drain electrodes.
Nowadays, several examples have been reported concerning the realization of all organic FETs, where flexible plastic foil is generally used as flexible substrate, a polymeric gate dielectric (PVA or PVP or PMMA) is used instead of SiO_2, and conductive polymers are employed as alternative to metals for the patterning of the electrodes [12].

1.5 6,13-Bis(triisopropylsilylethynyl)pentacene

Acenes are a class of hydrocarbons consisting of a numbers of benzene rings; the Pentacene ($C_{22}H_{14}$) belong to this class and, as is clear from name, it consist of five benzene rings (see Figure 1.12 (a)). This molecule is the basis of the most important organic semiconductor that are used for the manufacture of OFET (Organic-Field-Effect-Transistor). Despite this, e Pentacene is not an ideal material: its solubility is not appreciable, vacuum process are needed to deposit it, it oxidize easily and disturbs the transport and the crystallization process in the devices. Also it can condense in two crystalline phases which do not mate perfectly; for this reason often in the device grains are created which decrease the device performance. One of the most common way to solve these problems is tying to the Pentacene groups of molecules to get so many types of molecules including TIPS-Pentacene (6,13-Bis(triisopropylsilylethynyl)pentacene) (Figure 1.12 (b)).

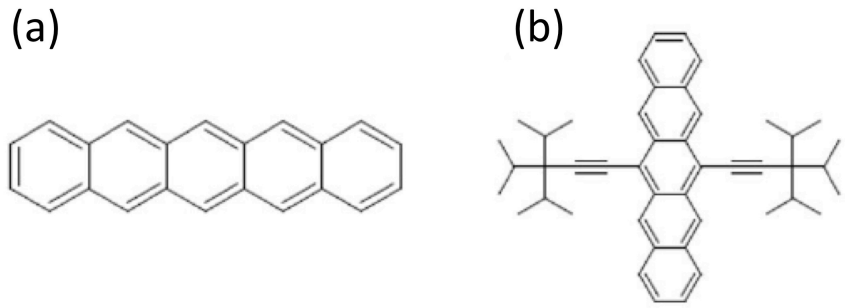

Figure 1.12: (a) Pentacene molecule, (b) TIPS-Pentacene molecule.

The TIPS-Pentacene is soluble in a wide variety of organic solvents and oxidize goes more slowly then Pentacene: when is in solutions it remains stable in air for days and when it is in form of crystals remains stable for weeks. The problem of such a molecule is that it has randomly organization, for this reason deposition techniques are necessary to arrange the crystals in an orderly manner to increase the mobility.

1.6 Poly(3-hexyl)thiophene (P3HT)

Thiophene-based conjugated polymers have accompanied, if not originated, the interest in conductive polymer materials and their application in organic field-effect transistors (OFETs) and organic photovoltaic (OPV) devices. The most studied representative of this class of materials is poly(3-hexyl-thiophene) (P3HT) with its regioregular (head-to-tail) isomer.

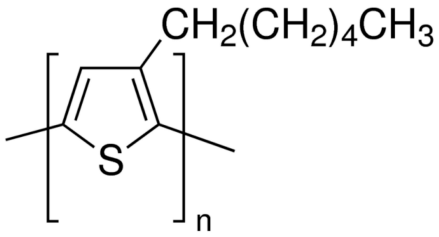

Figure 1.13: poly(3-hexyl-thiophene) (P3HT).

The first polymerization reactions with high yield and small concentrations of synthesis impurities were reported in 1980. Solution-processed into thin films, these materials could exhibit reasonable conductivities limited, however, by the disorder that results from a regiorandom attachment of the side chains to the thiophene monomers. Like many conjugated polymers, P3HT is a polymorph, i.e., forms different crystal structures depending on processing conditions.

The most frequently observed are so-called forms I and II, which differ by the side chain conformation and interdigitation, inclination of conjugated backbones with respect to the stacking direction, and the shift of successive (along the π-stacking direction) polymer chains. Form I, which is observed after annealing, is the structure encountered in most studies dealing with OFETs and OPVs.

On a mesoscale, crystallization from supercooled solutions in poor solvents can lead to the formation of secondary structures, notably nanofibers, with a width of tens of nanometers and length of several micrometers. OFETs active layer with P3HT may be sensitive to some wavelengths of light in the presence of oxygen. While this is not an acute problem for the bulk material, solutions and thin films tend to show some sensitivity over time. Therefore, storage and handling in an inert atmosphere (like nitrogen or argon) is recommended.

2 Kelvin Probe Force Microscopy

Kelvin probe force microscopy, or KPFM, was introduced as a tool to measure the local contact potential difference between a conducting atomic force microscopy (AFM) tip and the sample, thereby mapping the work function or surface potential of the sample with high spatial resolution. Since its first introduction by Nonnenmacher et al. in 1991[13], KPFM has been used extensively as a unique method to characterize the nano-scale electronic/electrical properties of metal/semiconductor surfaces and semiconductor devices. Recently, KPFM has also been used to study the electrical properties of organic materials/devices [14][15] and biological materials [16][17].

This chapter presents the principles and theory of KPFM and explores the use of nanometer resolution KPFM to characterize the electrical properties of semiconductor materials/devices. KPFM is used in this experimental work to image potential distributions on the surface with nanometer resolution, for characterizing the electrical properties samples investigated.

Fundamental to stable operation in KPFM mode is a relibable interaction of the AFM-tip with the sample topography in non-contact mode. Hence in the following paragraph I describe the basic principle of non-contact mode AFM operation and then turn to the details of KPFM.

2.1 AFM in non-contact mode

The working principle of non-contact mode exploits the attractive force between a tip and the sample surface [18]-[19]. The interactive force between a tip and a sample as a function of distance can be qualitatively evaluated considering the van der Waals forces. In fact considering the Van der Waals potential energy of two atoms, separated by a distance *r*, we can get the Lennard-Jones potential useful to achieve the energy of interaction and finally the interactive force. The Lennard-Jones potential is given by equation:

$$U_{LD}(r) = U_0 \left\{ -2 \left(\frac{r_0}{r} \right)^6 + \left(\frac{r_0}{r} \right)^{12} \right\} \qquad \textbf{(2.1)}$$

in which the first term of the sum represents the long-distance attraction caused, mostly, by dipole-dipole interaction, the second term describes the short range repulsion due to the Pauli exclusion principle and r_0 is the distance at which the potential reaches its minimum, thus it represents the equilibrium distance between atoms. This equation describes the behaviour of the tip to be attracted by the surface at large distances while repelled at small distances.

The energy of interaction is given by:

$$W_{PS} = \int_{V_P} \int_{V_S} U_0 \, n_s(r) n_t(r) dV dV' \tag{2.2}$$

Where $n_s(r)$ and $n_t(r)$ are relatively the densities of atoms in the sample and in the tip. Then the force between the tip and the sample surface can be calculated operating the gradient of the energy obtained in equation (2.2):

$$F_{PS} = -grad(W_{PS}) \tag{2.3}$$

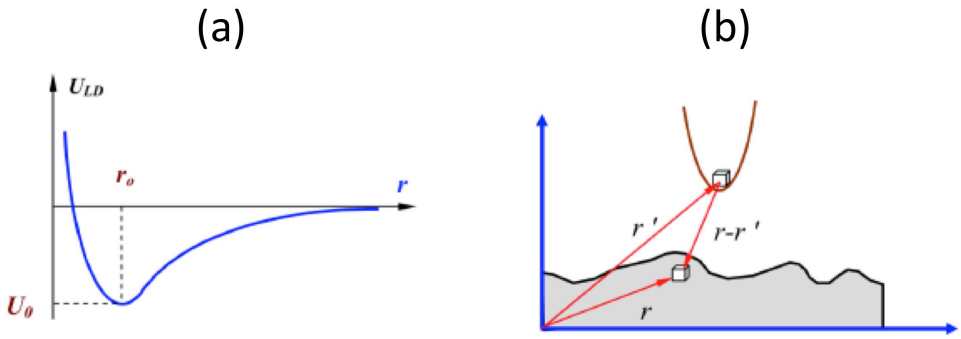

Figure 2.1: (a) dependence of the Lennard-Jones potential U_{LD} of atomic interaction on the distance r between the atoms. (b) Representative way to calculate the energy of interaction between tip and sample atoms.

This force can be measured by monitoring the cantilever deflection that is quantified by the measurement of a laser beam that is reflected off the backside of the cantilever and onto the Position Sensitive Photo Detector (PSPD), which is a four-section split photodiode (see Figure 2.2).

The sample is located on a piezo tube scanner, which can move the sample in the horizontal direction (X-Y) and in the vertical direction (Z). The PSPD establishes a feedback loop which controls and coordinates the piezo tube scanner vertical movement across the sample surface in order to maintain the tip at a constant force, to achieve height information, or at a constant height, to achieve force information.

More in detail, as the tip scans the sample surface, the cantilever bends depending on the roughness of the surface resulting in different light paths which causes the amount of light in the two photodetector sections. The difference in light intensities between the two sections (the upper and the lower part of the photodetector) is compared in a differential amplifier and the signal is converted into a voltage that enables the maintenance of the required values. When the fixed values to maintain are the force (force constant mode), the piezoelectric scanner controls height deviation in real time, while when we operate in height constant mode the deflection force of the sample is monitored. The piezoelectric

scanner allows AFM to reach 1 nm of lateral resolution. In vacuum conditions, atomic resolution has been achieved vertically for hard materials.

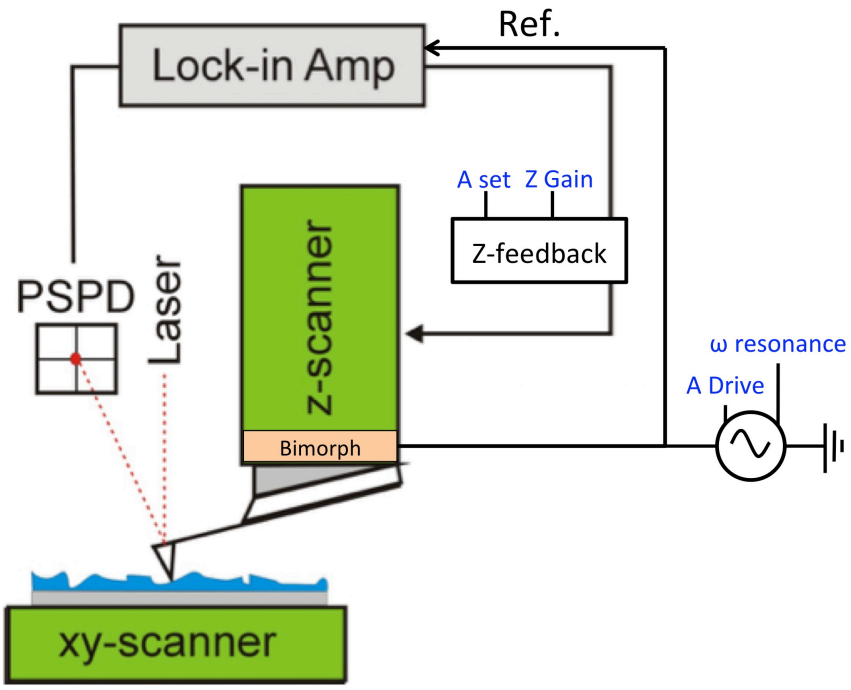

Figure 2.2: Block diagram of AFM system.

When the distance between the probe tip and the sample atoms is relatively large, like in non-contact mode, the attractive force F_{el} becomes dominant. Ion cores become electric dipoles due to the valence electrons in the other atoms, and the force induced by the dipole-dipole interaction is the van der Waals Force. Non-contact AFM (NC-AFM) measures surface topography by utilizing this attractive atomic force in the relatively larger distance between the tip and a sample surface. Using a feedback loop to monitor these changes, due to attractive Van der Waals forces between the tip and the sample at each (x,y) data point, the surface topography can be measured.

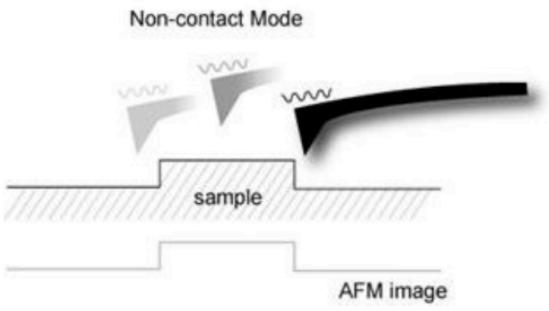

Figure 2.3: Concept diagram of non-contact mode.

Unlike contact-mode, non-contact AFM does not require a direct contact with the sample. In Non-Contact mode, the force between the tip and the sample is very weak so that there is no unexpected change in the sample during the measurement. This kind of measurement has the advantage that soft sample can be investigated and the tip will also have an extended lifetime because it is not abraded during the scanning process. On the other hand, the force between the tip and the sample in the non-contact regime is very low, and it is not possible to measure the deflection of the cantilever directly. So, Non-Contact AFM detects the changes in the phase or the vibration amplitude of the cantilever that are induced by the attractive force between the probe tip and the sample while the cantilever is mechanically oscillated near its resonant frequency.

A cantilever used in Non-Contact AFM typically has a resonant frequency between 100 kHz and 400 kHz with vibration amplitude of a few nanometers. Because of the attractive force between the probe tip and the surface atoms, the cantilever vibration at its resonant frequency near the sample surface experiences a shift in spring constant from its intrinsic spring constant (k_0). This is called the effective spring constant (k_{eff}), and the following equation holds:

$$k_{eff} = k_0 - F' \tag{2.4}$$

When the attractive force is applied, k_{eff} becomes smaller than k_0 since the force gradient F' ($=\partial F/\partial$) is positive. Accordingly, the stronger the interaction between the surface and the tip (in other words, the closer the tip is brought to the surface), the smaller the effective spring constant becomes. This alternating current method (AC detection) makes more sensitive responds to the force gradient as opposed to the force itself.

A bimorph is used to mechanically vibrate the cantilever. When the bimorph's drive frequency reaches the vicinity of the cantilever's natural/intrinsic vibration frequency (f_0), resonance will take place, and the vibration that is transferred to the cantilever becomes very large. This intrinsic frequency can be detected by measuring and recording the amplitude of the cantilever vibration while scanning the drive frequency of the voltage being applied to the bimorph.

The spring constant affects the resonant frequency (f_0) of the cantilever, and the relation between the spring constant (k_0) in free space and the resonant frequency (f_0) is as in equation (2.5) :

$$f_0 = \sqrt{\frac{k_0}{m}} \tag{2.5}$$

As in equation (2.4), since k_{eff} becomes smaller than k_0 due to the attractive force, f_{eff} too becomes smaller than f_0 as shown in Figure 2.4 (a).

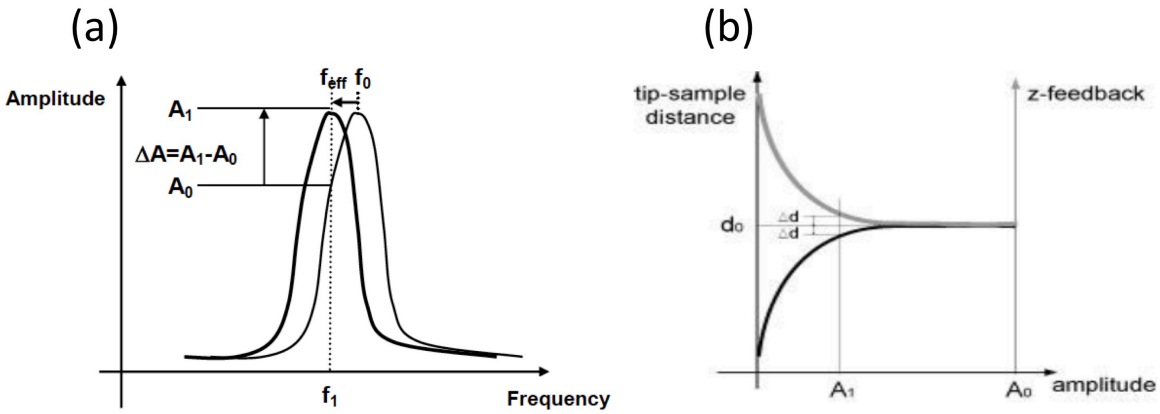

Figure 2.4: (a) Resonance frequency shift, (b) Amplitude vs Z-feedback.

If you vibrate the cantilever at the frequency f_1 (a little larger than f_0) where a steep slope is observed in the graph representing free space frequency vs. amplitude, the amplitude change (ΔA) at f1 becomes very large even with a small change of intrinsic frequency caused by atomic attractions. Therefore, the amplitude change measured in f1 reflects the distance change (Δd) between the probe tip and the surface atoms.

If the change in the intrinsic frequency resulting from the interaction between the surface atoms and the probe or the amplitude change (ΔA) at a given frequency (f_1) can be measured, the non-contact mode feedback loop will then compensate for the distance change between the tip and the sample surface as shown in Figure 2.4. By maintaining constant cantilever's amplitude (A_0) and distance (d_0), non-contact mode can measure the topography of the sample surface by using the feedback mechanism to control the Z scanner movement following the measurement of the force gradient represented in equation (2.4)[18].

2.2 electrostatic force microscopy

Before considering details of microscopic methods, it is important to understand the principles of electronic energy levels at the heart of electrostatic force microscopy (EFM) and Kelvin-probe force microscopy (KFM or KPFM; also SKPM is used, for scanning Kelvin-probe microscopy). Figure 2.5 depicts an idealized tip-sample system (ignoring the possible effects of a cantilever). If we bring together two dissimilar metallic materials (tip and sample) that are not electrically grounded, their electronic vacuum (energy) levels become the same (Figure 2.5 (a)). In general, the two Fermi energy levels (the highest energy of occupied electronic states) are different. If tip and sample are metallic, the difference of vacuum to Fermi level is the work function. Upon electrically connecting the

materials and assuming an adequate number of moving electrons, a substantial displacement of electron charge will act to align Fermi levels and offset vacuum levels (Figure 2.5 (b)).

This produces an electric field between tip and sample and thus a net force of attraction between opposite charges, as well as charge-dipole attractive forces[20].

Applying an appropriate external bias between tip and sample can generate a larger total tip-sample voltage difference, enhancing the strength of attraction and its possible variation from point to point along the surface (e.g., if heterogeneous in dielectric constant). This additional external bias may be needed to generate adequate image contrast EFM.[2] Alternatively, by connecting just the right dc voltage offset between the two materials, the vacuum levels can be brought into alignment and thus the force eliminated or nulled. To achieve this condition the applied voltage must be equal and opposite to the surface potential difference of the (commonly grounded) materials, also know as the contact potential (or contact potential difference, V_{cpd}). If the work function of the tip ϕ_t is greater than that of the sample ϕ_s, then a positive tip voltage would be needed in order to drop the energy levels (of negatively charged electrons) to achieve the nulling state (Figure 2.5 (c)). In KFM, one wishes to map this applied voltage across the surface to obtain a contact potential image.

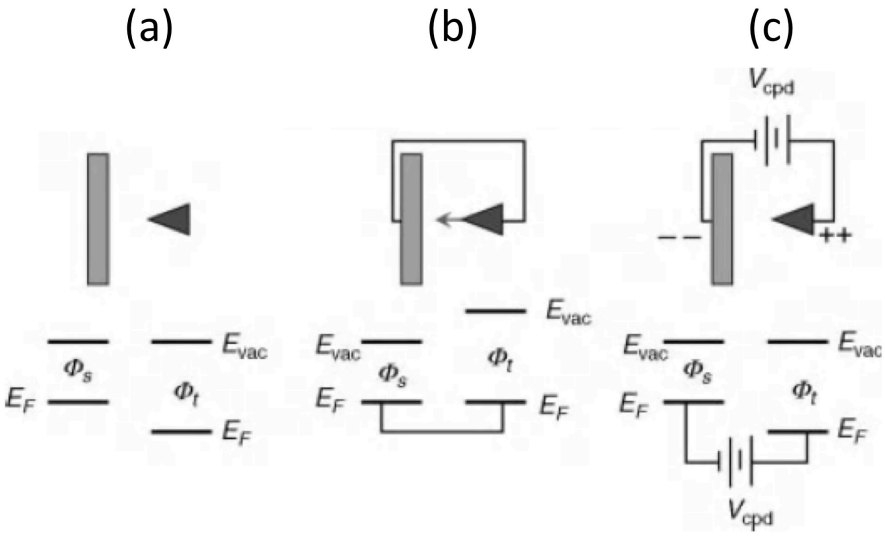

Figure 2.5: idealized tip and sample electronic energies at the vacuum level and Fermi level, for the case of dissimilar work function. Materials that are (a) not electrically grounded, (b) electrically grounded (common), and (c) electrically connected with a battery in between, of the exact potential difference needed to match the work-function difference and thus align vacuum levels.

[2] One should bear in mind that large biases, of order several volts, can change the electron energetics in the sample such that the method cannot be considered a "weakly perturbative" probe of sample properties. In physicists' language, perturbation or linear response theory does not apply, that is, the Hamiltonian of the system is being substantially modified by the strong electric field.

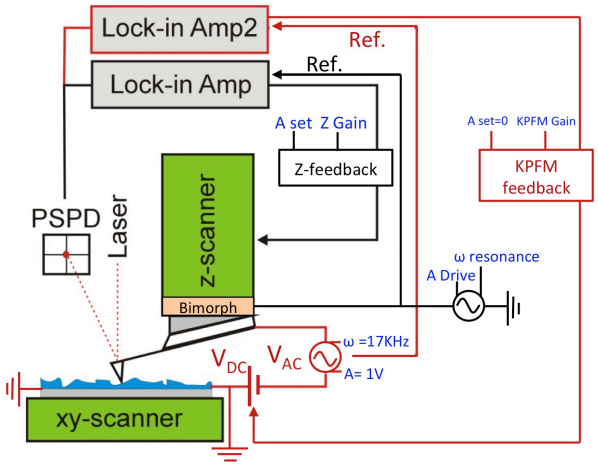

Figure 2.6: Block diagram of KPFM mode AFM system.

In order to realize a scanning technique which is sentitive to the surface potential the following approach is pursued: an AC voltage (V_{AC}) plus a DC voltage (V_{DC}) is applied to the AFM tip. V_{AC} generates oscillating electrical forces between the AFM tip and sample surface, and V_{DC} is then adjusted in a feedback cycle to nullify the oscillating electrical forces that originated from CPD between tip and sample surface. In detail the electrostatic force (Fes) between the AFM tip and sample is given by:

$$F_{es} = \frac{1}{2}\Delta V^2 \frac{dC(z)}{dz} \qquad \textbf{(2.6)}$$

where z is the direction normal to the sample surface, ΔV is the potential difference between V_{CPD} and the voltage applied to the AFM tip, and dC/dz is the gradient of the capacitance between tip and sample surface. When $V_{AC}\sin(\omega t) + V_{DC}$ is applied to the AFM tip, the voltage difference ΔV will be:

$$\Delta V = V_{tip} \pm V_{CPD} = (V_{DC} \pm V_{CPD}) + V_{AC}\sin(\omega t) \qquad \textbf{(2.7)}$$

Note that the ± sign depends whether the bias (VDC) is applied to the sample (+) or the tip (−). Substituting equation (2.7) in equation (2.6) gives the expression of the electrostatic force applied to the AFM tip:

$$F_{es}(z,t) = -\frac{1}{2}\frac{\partial C(z)}{\partial z}[(V_{DC} \pm V_{CPD}) + V_{AC}\sin(\omega t)]^2 \quad \textbf{(2.8)}$$

This equation can be divided into three parts following basic trigonometric identity $sin^2x = \frac{1-cos2x}{2}$:

$$F_{DC} = -\frac{\partial C(z)}{\partial z}\left[\frac{1}{2}(V_{DC} \pm V_{CPD})^2\right] \quad \textbf{(2.9)}$$

$$F_{\omega} = -\frac{\partial C(z)}{\partial z}(V_{DC} \pm V_{CPD})V_{AC}\sin(\omega t) \quad \textbf{(2.10)}$$

$$F_{2\omega} = \frac{\partial C(z)}{\partial z}\frac{1}{4}{V_{AC}}^2[\cos(2\omega t) - 1] \quad \textbf{(2.11)}$$

F_{DC} (Equation (2.9)) results in a static deflection of the AFM tip. F_{ω} with frequency ω (Equation (2.10)) is used to measure the V_{CPD}, and $F_{2\omega}$ (Equation (2.11)) can be used for capacitance microscopy.

When electrostatic forces are applied to the tip by V_{AC} with V_{DC} , additional oscillating components (due to the electrical force) will be superimposed to the mechanical oscillation of the AFM tip. A lock-in amplifier is employed to measure the V_{CPD}, to extract the electrical force component with frequency ω (F_{ω}), a function of V_{CPD} and V_{AC}. The output signal of the lock-in amplifier is directly proportional to the difference between V_{CPD} and V_{DC}. The V_{CPD} value can be measured by applying V_{DC} to the AFM tip, such that the output signal of the lock-in amplifier is nullified and F_{ω} equals zero. Subsequently, the value of V_{DC} is acquired for each point on the sample surface, composing a map of the work function or surface potential of the whole sample surface area.

KPFM measures topography concurrently with V_{CPD}, using an AFM tip. A method to separate the topographical signal from the V_{CPD} measurement is required.

SKPM exploits the non-contact regime of probe-sample interaction and allows to map the sample topography and surface potential in concomitantly. To stabilize performance in the attractive regime, the cantilever is driven at a frequency alightly larger than the fundamental resonant frequency, and the set point amplitude is about 90% of the free amplitude. In this way the wear of the tip is minimized and a single cantilever is used for the full characterization of a sample at various strain values.

To probe the electrostatic forces, an AC bias of 1V amplitude at a frequency 17kHz was applied to the tip. The resulting tip oscillation is fed after lock-in amplification into a feedback loop which is

engaged to null the electrostatic interaction by adjusting a DC voltage offset applied to the tip. The resulting DC-voltage called surface potential V_{CPD} in the following, is recorded with the image topography.

3 Materials and Methods

Device models provide a common language for the discussion of the characteristics of transistor devices. The parameters measured in device characterization are the raw material with which the behavior of devices can be summarized using a few parameters and insights about the physical processes, which underlie OFET behavior, can be explained.
This chapter will highlight the typical TFT structure used in this experimental work (section 3.1). in section 3.2 techniques that allows to extrapolate the parameters for the transistor characterization will be described. Subsequently, in subsection 3.4, the way with which the device has been bent is presented. This includes also a description of the simulation technique applied to model the deformation in the ideal bended system. In section 3.4 the measurement KPFM setup and the choice of the parameters used are described. Methods for image analysis and image correction are detailed in section 3.5. Section 3.6 will describe the overall experimental protocol used for a complete bending experiment.

3.1 TFT structures

All OTFTs were fabrictated at *Department of Electric and Electronic Engineering, University of Cagliari, Piazza d'Armi, Italy by Stefano Lai, Piero Cosseddu and Analisa Bonfiglio.* In the process, the aluminum gate electrode was deposited through a shadow-mask on a 150 um thick film of 150μm thick Polyethylenenaphtalene (PEN) as substrate to result in 90 nm thickness. The ~6 nm thick film of Al2O3 layer is realized at room temperature by UV-ozone oxidation (using a mercury lamp, UVP PenRay) performed in ambient conditions for a maximum time of 1 h. 170 nm of Parylene C are deposited by chemical vapor deposition (CVD) (Specialty Coating Systems) at room temperature, using A174 as adhesion promoter. The specific capacitance of the dielectric was determined to be 16 nF/cm2. Thermally evaporated gold source and drain contacts (40 nm thickness) are realized on top of the Par C layer with a photolithographic process. The channel defined by these interdigitated electrodes amounts to length and width of L=26 μm and W = 23.12 mm, respectively.
6,13-Bis(triisopropylsilyle-thynyl)pentacene (TIPS) was deposited by drop casting from a 1% solution using anisole as organic solvent. Poly(3-hexyl-thiophene) was deposited by dropcasting from a solution of 1% in chlorobenzene. The cross section of the described device is shown in Figure 3.1 (b).

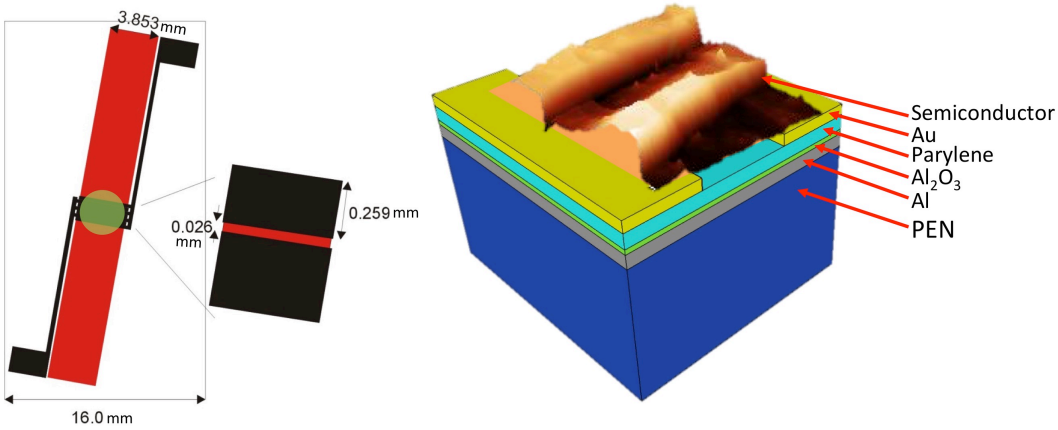

Figure 3.1: (a) top view of typical TFT used in these experiments. (b) The cross section of the TFT shows the amount and types of different layers used. Scale is not respected.

3.2 Transistor Characterization

Besides its technological interest, the thin-film transistor is also a tool of choice to analyze charge injection and transport in organic semiconductors. In that respect, methods for extracting the basic parameters are of crucial importance. Equations (1.13) and (1.14) are the premise for the most popular methods for mobility extraction[11].

The probably most widespread one makes use of the transfer characteristic in the saturation regime, and this is the regime in which we conducted experiments.

A Keysight B2912A sourcemeter, was used to provide the V_{DS} potential and measure the drain current ID. V_G potential is set by the AFM electronics and is applied to the sample holder of the instrument and further wired to the Al-gate electrode. The transfer characteristic was taken in saturation regime, at V_{DS}=-5V while V_G potential is swept from -3V to 3V for a period of 10 seconds. The output characteristic was taken varying V_D from 0V to -5V with steps of ΔV_D=0.1V and varying V_G from 2V to -5V with steps of ΔV_G=1V.The Smucs software created by Dr. Tobias Cramer, researcher in the University of Bologna, acquired all the data.

All relevant parameters like mobility and threshold voltage were calculated from these acquired data with the formula described in

(3.1). In practise these parameters were extrapolated from the linear fit of $\sqrt{I_D}$ versus V_G graph (example in Figure 3.2 (b)).

More precisely, the square root of the drain current is plotted as a function of the gate voltage. The principle of the method can be illustrated by rewriting equation (1.14) as

$$\sqrt{I_{Dsat}} = \sqrt{\frac{W}{2L} C_i \mu [V_G - V_T]} \qquad \textbf{(3.1)}$$

(3.1) predicts a straight line; the mobility is obtained from the slope of the line, while the threshold voltage corresponds to the extrapolation of the line to zero current.

However, this method presents a critical drawback. In the saturation regime, the density of charge varies considerably along the conducting channel, from a maximum near the source to practically zero at the drain. As will be seen in the following, the mobility in organic semiconductors is not constant; rather, it largely depends on various parameters, including the density of charge carriers. A direct consequence of this is that in the saturation regime, the mobility is not constant along the channel, and the extracted value only represents a mean value and instead of a straight line a curvature is observed at voltages close to threshold. For this reason, I select a rage of higher Vg-values where (3.1) is valid and I can consider μ constant, so I'm interested in the part of curve where the slope is constant.

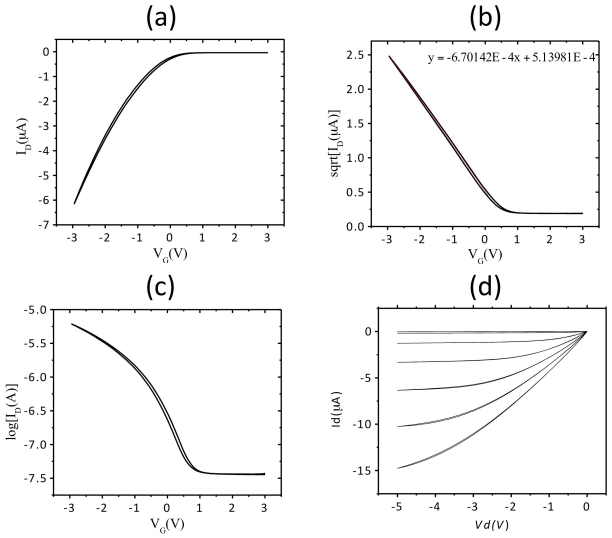

Figure 3.2: Representative transfer (a)(c) and output characteristic output (d) of organic transistor. The fit in (b) is is used for calculate the mobility μ and the threshold voltage V_{TH}.

The off current I_{OFF} was determined using the graph Log(I_D) versus V_G. I_{OFF} current was calculated by the mean value in the pinch-off condition), in the $1.5V<V_G<2.5V$ range.

3.3 Deformation of TFT

One key advantage of organic electronic devices is the possibility to produce flexible all-organic OTFTs with the functional organic semiconductor films deposited on flexible plastic foils like Mylar or Polyethylenenaphtalene (PEN, which has been studied in this chapter) as substrate.

In this chapter is reported how the device is mounted in the sample carrier, how it is possible to apply different strains to substrate and a description of the experimental setup for the TFT characterization under strain.

Subsequently simulation of mechanical deformation technique that was elaborated by *Stefano de Miranda* and *Luca Patruno* from the *Department of Civil, Chemical, Environmental, and Materials Engineering*. *Alberto Costa* has designed and manufactured the sample carrier support at the mechanical workshop of the Department of Physics and Astronomy that is mounted into the AFM.

3.3.1 Setup for mechanical deformation

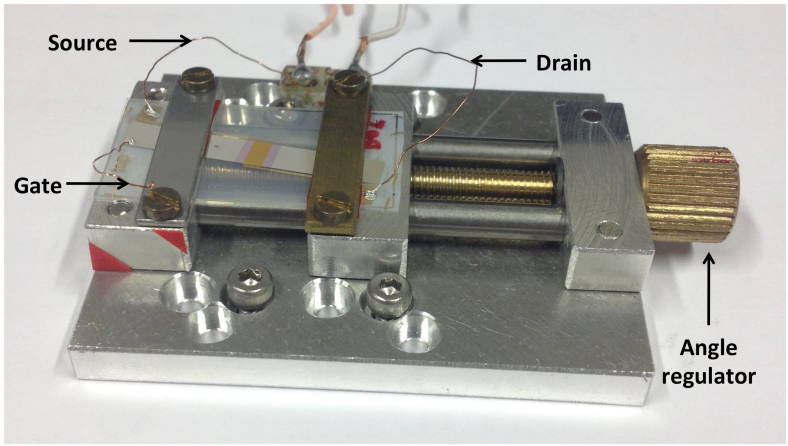

Figure 3.3: the image show how the sample is mounted in to sample carrier, with relative electrical connections. Turning the screw, it is possible to modify the mechanical stress applied to the device.

As shown in Figure 3.3 the edges of the plastic substrate are fixed on the armatures of a bending machine. When one armature is moved towards the other, the substrate is bent.

We have applied bending radii ranging from 12 mm down to 2 mm, corresponding to an induced surface strain from 0.4 % to 3.0 %.

All the measurements have been performed starting from the small deformation regime (large bending radii), and the deformation was constantly increased by reducing the bending radius.

Drain, source and gate contacts have been made with silver paste, in particular gate is connected directly to the metallic sample holder, whose base is directly connected to the AFM sample bias generator. So it is possible to set up the V_G potential directly from the control panel of the AFM varying the sample bias voltage.

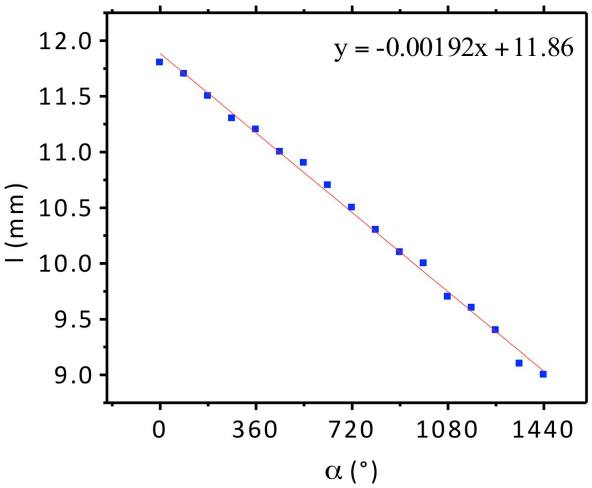

Figure 3.4: Calibration curve used to calculate l, from the rotation screw angle α.

The calibration curve shown in Figure 3.4 was made from the experimental points, was used to calculate the distance between the two armatures of the sample carrier (l) from the rotation angle of the adjustment screw.

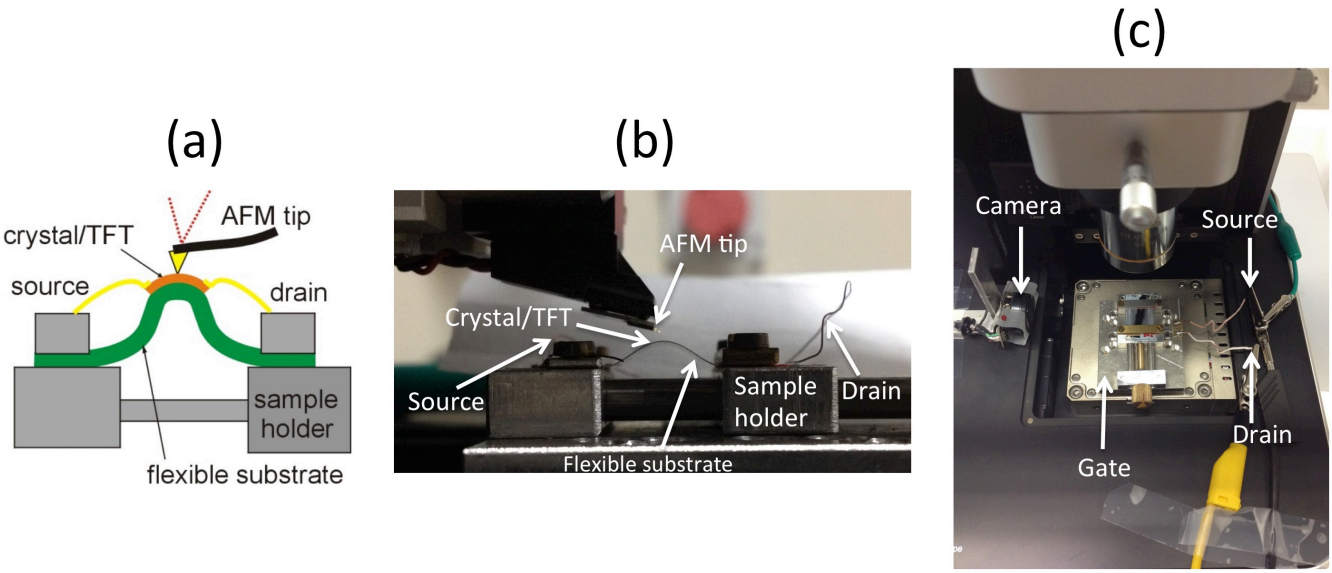

Figure 3.2: (a) the scheme shows the AFM tip approach on the surface, (b) a lateral image shows the real apparatus for measuring under bending, (c) measurement setup for KPFM measurement, with relative electrical connections. The camera is used to take lateral images every step of bending.

The entire experimental setup employed for the electromechanical characterization is reported in Figure 3.2. The camera is used for take picture before every bending step, to determine subsequently the radius of curvature and obtain the strain value each bending step.

3.3.2 Simulation of mechanical deformation

As a first step toward the numerical modelling of the device, a simple system composed of a straight beam clamped at both ends has been considered. The system has been modelled by using the standard Finite Element Method in the commercial software Straus7. The bar has been discredited by using 40 finite elements and a non-linear analysis has been performed in order to take into account geometric non-linearities. An overview of the configurations assumed by the flexible bar with increasing dL/L is reported in Figure 3.5.

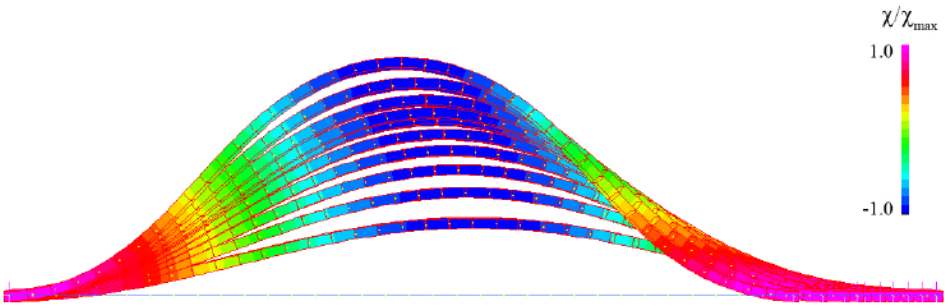

Figure 3.5: Congurations assumed by the fexible bar with increasing displacements coloured by the ratio between the local and the maximum curvature (the maximum curvature (max) is calculated separately for each conguration).

3.4 Kelvin Probe Force Microscopy

Kelvin probe force microscopy measurements were obtained by means of a Park Atomic Force Microscope NX10 in non-contact mode equipped with PPP-NCST Au probes (Nanosensors). XEP data acquisition program for XE series SPM was used to interface to the microscope [21].

Drain-source current (I_D) measurements were carried out at room temperature in air. A Keysight B2912A sourcemeter, was use for give the V_{DS} potential. V_G potential is given directly from the AFM by acting the simple bias voltage. Figure 3.6 shows the experiment electric scheme with the applied potentials.

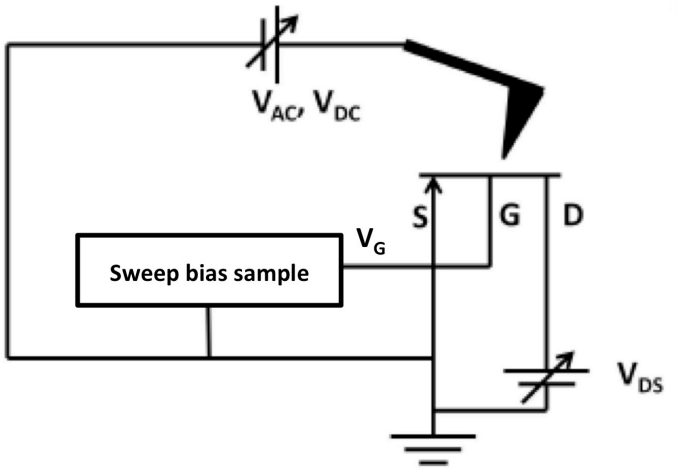

Figure 3.6: OFET electric scheme with the applied potentials.

Before approach with the tip to acquire the image, positioning at the highest point of the bended TFT must be assured. To achieve this, by optical microscope of AFM, the coordinates of four points in the TFT substrate (i.e. the four corners inside the armatures) where determined by optical microscopy and by moving the sample in the xy system by a micropositioning system. Based on these coordinates the centerline of the TFT, that will be at the maximum height during bending was calculated.

After approaching, AFM and KPFM parameters must be optimized. Typically KPFM parameters used are:

- **Drive**: controls the strength of the drive amplitude used for the cantilever vibration. The drive amplitude is the amplitude of the AC voltage signal from the signal wave generator that drives the bimorph piezoelectric to vibrate. This number is a fixed percentage (from 1 to 100) of the maximum allowed voltage to the piezoelectric transducer which oscillates the cantilever. It was set in order to have a vibration amplitude of about 30nm.
- **Set point**: specifies the reference signal of the feedback loop. In Non-Contact mode, set point specifies a value for the amplitude of the cantilever's vibration. Usually it was set to 90% of amplitude peak at the cantilever resonance frequency;
- **Tip Bias**: applies a bias voltage to the tip. It was set to V_{AC} = 2V.
- **Z servo Gain**: controls how much the error signal in the feedback loop is amplified before used to generate a feedback voltage to the scanner and therefore changes Z scanner feedback sensitivity. Usually was set to 1÷3;
- **Sample Bias**: set VG applied to the transistor. (in these experiment V_G=-3V).
- **Adaptive scan**: is feedback system which acquires new scan rate from error signal. Maximum scan rate was set to 0.3 Hz, minimum scan rate was set to 0.03Hz with step 0.03Hz.

- **Scan size**: indicates the width of the scan. Usually was set to 45μm or 2μm for detailed indagations.
- **Tip bias servo**: in these experiments was set to 10;

After parameter optimization, and transistor activation, AFM scans were taken. Usually images of size 128x128 and 256x256 pixels were taken. A resolution of 256 pixels each line is used for image more detailed, to investigate in more detail morphology and surface potential aspects.

3.5 Image analysis

To analyse the AFM and KPFM images, the Gwyddion software [22], that is a modular program for SPM data visualization and analysis of height fields obtained by scanning probe microscopy techniques, is used. In this work AFM was useful to determinate if the substrate morphology under mechanical stress changes, and with the KPFM mode, it is possible to investigate surface potentials variation.

Before achieving these information, the acquired images were submitted to a common procedure in order to correct know artifacts in AFM images.

Image ".tiff" were opened with Gwyddion software and then a series of common commands were selected, to reduce typical experimental problems that make images less sharp and less clear to analyse.

The common procedure consists in levelling the image, and change the contrast by set the colour range and edit color maps. For leveling the image, three-point leveling command was used. It require to select a datum plane and the software determines automatically the average curvature and slope of the image. Then, the software calculates a set of values that will compensate for the slope. Finally, you can have the software subtract the compensating values from the data points of the image. Artifacts can be removed by remove of data under arbitrary mask using Laplace or fractal interpolation.

Gwyddion was used also to extract profiles from the images, measure distance, and for 3D data display with false colour representation. In the next chapter all these application will be study in deep, with the consequent physical considerations.

3.6 Experimental protocol

Since this type of experiment has never been done so far, in following the procedure used in the experimental work will be exposed.

After sample mounting, it is necessary to set the AFM and KPFM parameters (see chapter 3.4)
These parameters will be changed during scanning images, to obtain sharper images, with little noise as possible. After image acquisition, the parameters will be reset to the default parameters.
Step that will be repeated for different degree of mechanical strain includes a bending procedure that allow to choice of the strain applied by turning the screw (usually increment of 45° 90° or 180° were applied) and a profile picture of the bended device was taken with the aim of obtaining the radius of curvature with a pattern recognition program (as it will be described in the next chapter).
The start experiment time was saved for having a reference experiment timeline and darkness was keeping as long as possible, because many carriers can be generated in the device and electrical measurements may not be reliable. This sensitivity to light may also degrade the device performance in time.
After approaching the sample, adjusting KPFM parameters by monitoring the line scan in the control panel of microscope (see Figure 3.7).

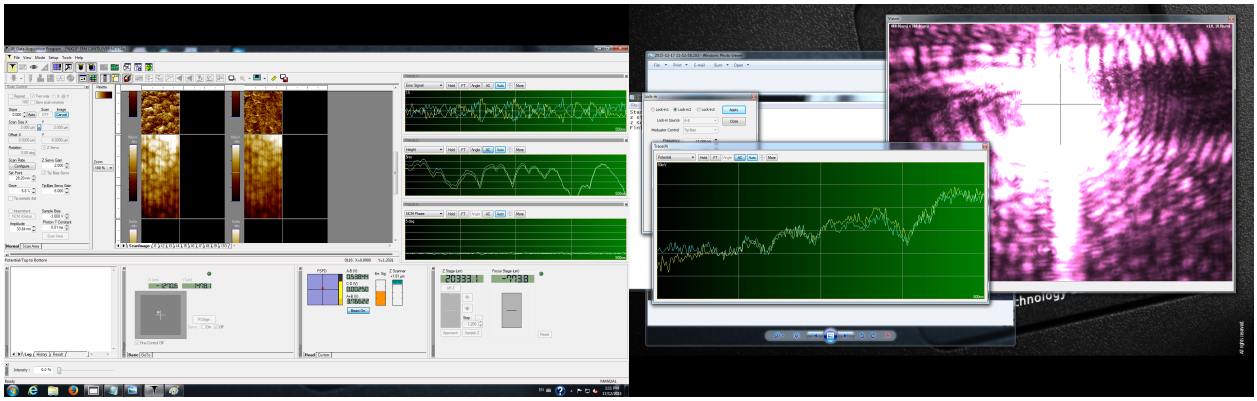

Figure 3.7: XEP data acquisition program for XE series SPM.

The transistor can be operate by applying V_G and V_D voltage. V_G is set using the sample bias voltage in the control panel of microscope and V_D is set using the Keysight B2912A sourcemeter using the appropriate Smucs interface program. After that its possible to acquire images.
It is necessary turn away the tip (usually 1 mm) to avoid the impact of the tip on the surface in the next bending step, where the strain will be increased.
To obtain the transfer curves the drain channel potential was set to -5 V by the Smucs control, and gate potential was varied from 3V to -3V for a period of 10 seconds, using the “sweep” control into “trace mode” microscope interfacing program. The finish time experiment was saved and a new bending step can be perform. The entire processes steps are summarizes as shows in Figure 3.8.

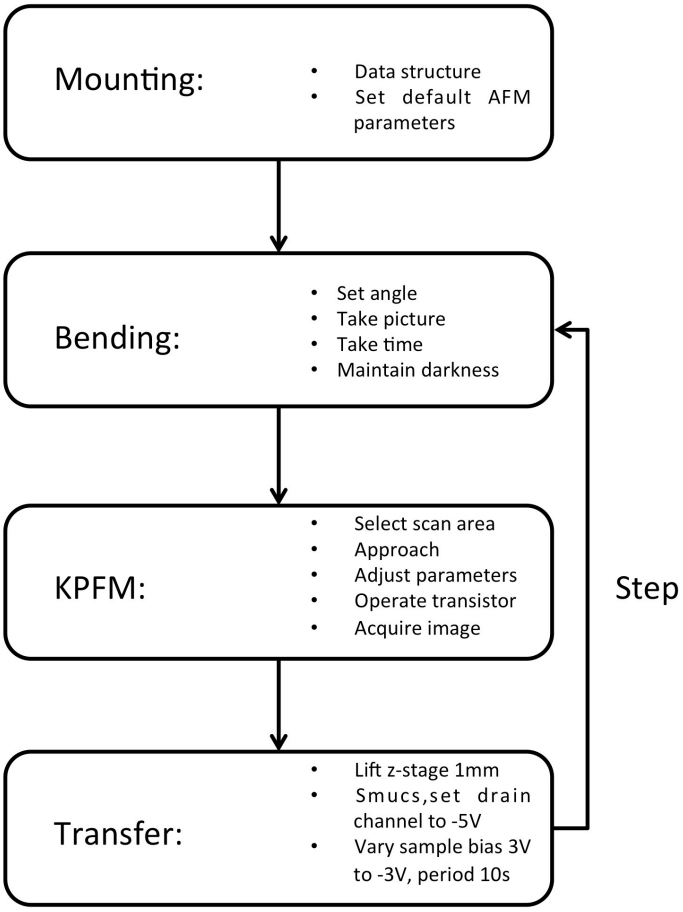

Figure 3.8: Flow chart that summarizes all the steps of the experiment.

4 Results and discussions

Here we report a comprehensive electrical characterization of flexible OTFT devices under applied bending-stress relating the macroscopic device characteristics to microscopic properties of the active layer, as determined by a combination of scanning force microscopy (SFM) and Kelvin Probe Force Microscopy (KPFM).

In section 4.1 I describe the mechanical deformation of TFT and how I extract experimentally the bending radius and calculate the strain ε. In section 4.2 I describe the case in which TIPS-Pentacene was used as active layer. First of all morphological and electrical consideration were made with unstressed device, after that mechanical strain was applied and resulting changes in morphology and surface potential are described. I correlate these local aspects in single microcrystals with the behavior of the device performance in terms of mobility μ, off-current I_{OFF}, and threshold voltage V_{TH}.

In section 4.3 the same consideration are made for a OTFT containing P3HT as active layer.

4.1 Mechanical deformation of TFT

To impose well defined strain to the active layer of the transistor, we induced a buckling deformation Using the configuration described in section 0, a uniaxial deformation is applied on the OTFT surface; the surface strain induced on the active layer may be evaluated using the following formula:

$$\varepsilon = \frac{d_l + d_s}{2R} \tag{4.1}$$

In which d_l and d_s are the thicknesses of the active layer and of the substrate respectively and R the bending radius.

Considering that the substrate is more than two orders of magnitude thicker than the active layer, the surface strain induced on the active layer can be approximated by:

$$\varepsilon = \frac{d_s}{2R} \tag{4.2}$$

Using the configuration described in section 3.3.1, the whole structure can be bent at different bending radii, and subsequently characterized electrically and by microscopy.

We have applied bending radii ranging from 2 mm to 12 mm, corresponding to an induced surface strain to 0.4% to 3%. All the measurements have been performed starting from small deformation

regime (large bending radii), and the deformation was constantly increased by reducing the bending radius.

The bending radius was estimated considering a homogeneous PEN foil, using a pattern recognition system, which identifies the device profile from the lateral image taken by the video camera (see Figure 4.1 (a)). The coordinates have been saved and were plotted, so that with a second order polynomial ($y=p_2x^2+p_1y+p_0$) fitting it was possible (Figure 4.1 (b)) to estimate the bending radius value of the bend sample by $r = \frac{1}{2p_1}$.

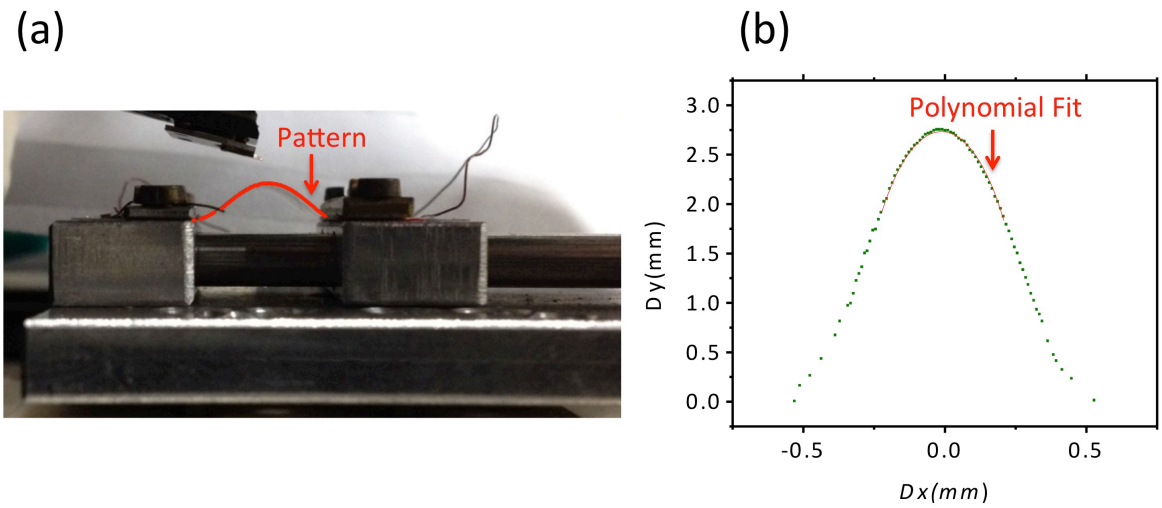

Figure 4.1: (a) lateral image of the bended TFT. In red it is shown how the pattern recognition system identifies the sample profile. (b) Digitalization of the pattern points made by the recognition system. In red it is shown the polynomial fit applied.

The height h of the bend device was determined from Z stage coordinates of the AFM head with the tip in interaction with the sample surface at the highest point of the sample as described in section 3.4. Figure 4.2 shows the experimental points taken with the pattern recognition technique and the difference with the simulations results. The difference between the two graphs is that the (a) curves were centred on the maximum value of height.

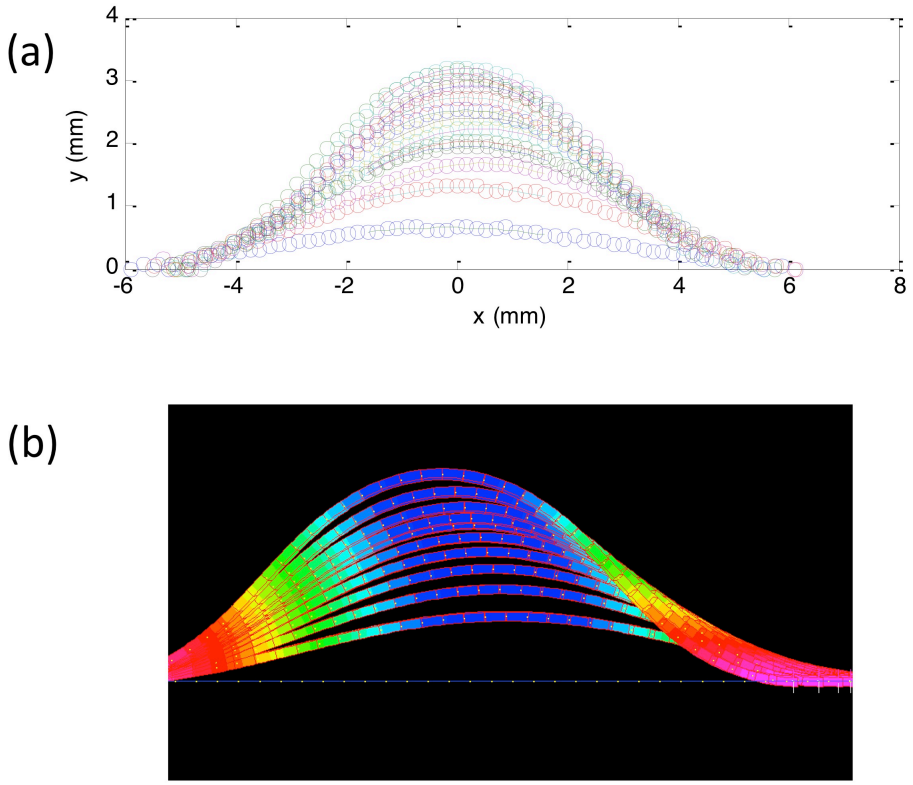

Figure 4.2: (a) the graph shows all the experimental pattern points made by recognition system for different step of bending. (b) Shows the simulated sample bending.

The extract value of R for various deformations compare well between device, substrate, and model as shown in Figure 4.3. This comparison shows that the entire mechanical behaviour is due to the substrate characteristics, in fact no significant differences between substrate and substrate with the device were found. The simulation confirms the result that there is no significant differences in macroscopic mechanical analysis.

For the range of R investigated here, we define an area in the top part of the bend device where strain can be considered constant, then in this area we patterned the active layer and electrodes of the device under test to guarantee homogeneous strain in the following experiments.

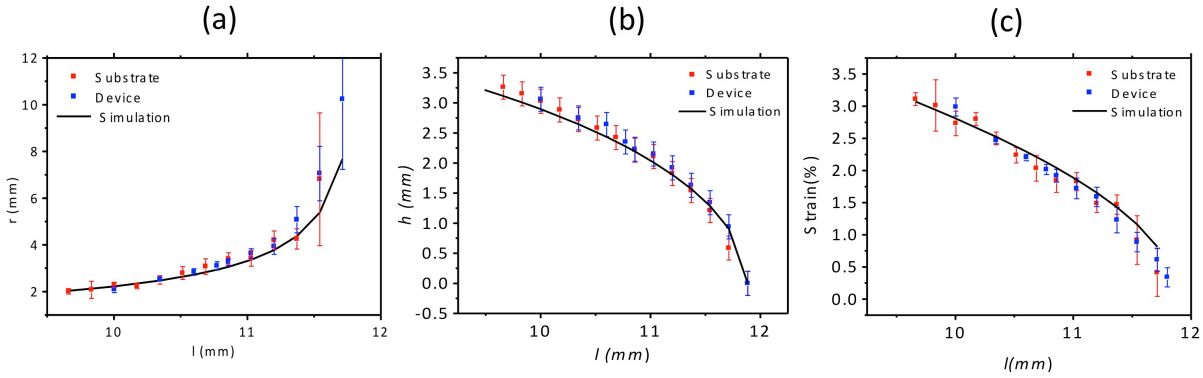

Figure 4.3: radius of curvature (a), height (b), strain (c) versus armature distance l for the substrate, substrate with TFT, and simulation.

4.2 TIPS Pentacene

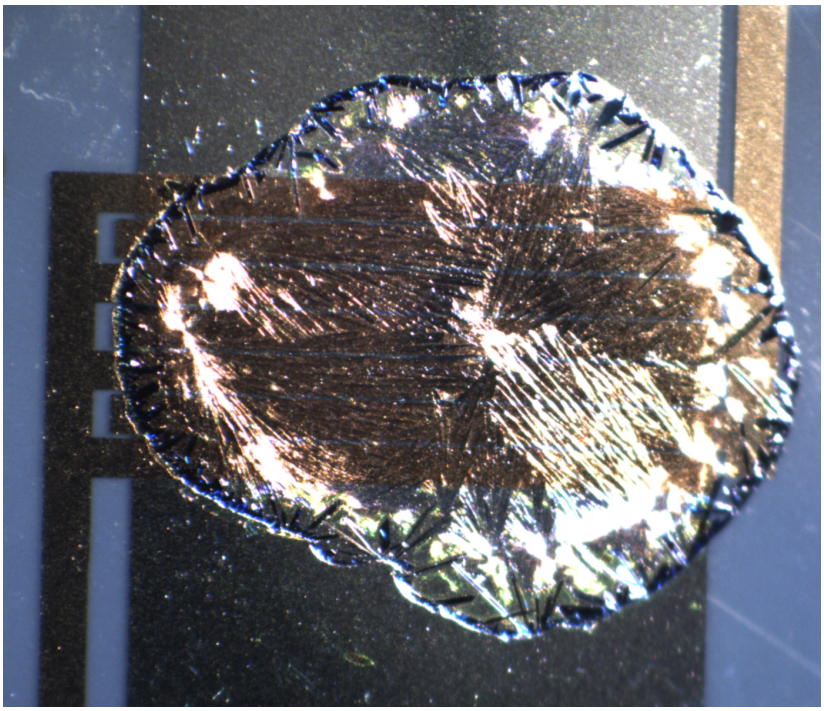

Figure 4.4: Image taken with the optical microscope showing the TIPS Pentacene crystals after the deposition process. Under the semiconductor layer is possible to see the interdigized electrode.

Figure 4.4 shows an optical micrograph of a typical OTFT contains TIPS-Penatacene as active layer. The picture clearly reveals the area covered by TIPS-Pentacene microcrystals as deposited by drop-casting. The hole interdigitated channel is covered by the organic semiconductor. The texture of the surface shows needly like patterns, which emerge from the formation of microcrystals, and their orientation of the crystals is purely random.

In this chapter the morphology and electrical characteristic of unstressed TIPS-pentacene TFT are investigated. Transfer characteristic were made, optical microscopy was used to identify the arrangement of the crystals, AFM microscopy is used to delineate the morphology of the crystals, and KPFM measurement was made to determinate electrical characteristic like work functions, surface potentials, etc.

After these measurements, I will focus in the analysis of particular areas, seeing what happens in terms of morphological and surface potential changes, when a mechanical strain is applied.

I measure transfer characteristic for each bending step and get the values of mobility μ, off current I_{OFF} and threshold voltage V_{TH}. We will discuss about μ, I_{OFF} and V_{TH} trends and we will find that crack generation is a crucial event that affects these trends.

4.2.1 unstressed tips pentacene TFT i-v characteristic and microscopic analysis

As one can see in Figure 4.5, crystals orientation is random. Then we focus the investigation on selected single crystals. With the optical microscope of NX10 we select the area of interest for our purposes. The choice of the crystal is arbitrary, but individual crystals have the common feature that they must connect the two gold electrodes crossing the TFT channel (the lighter stripe in the Figure 4.5).

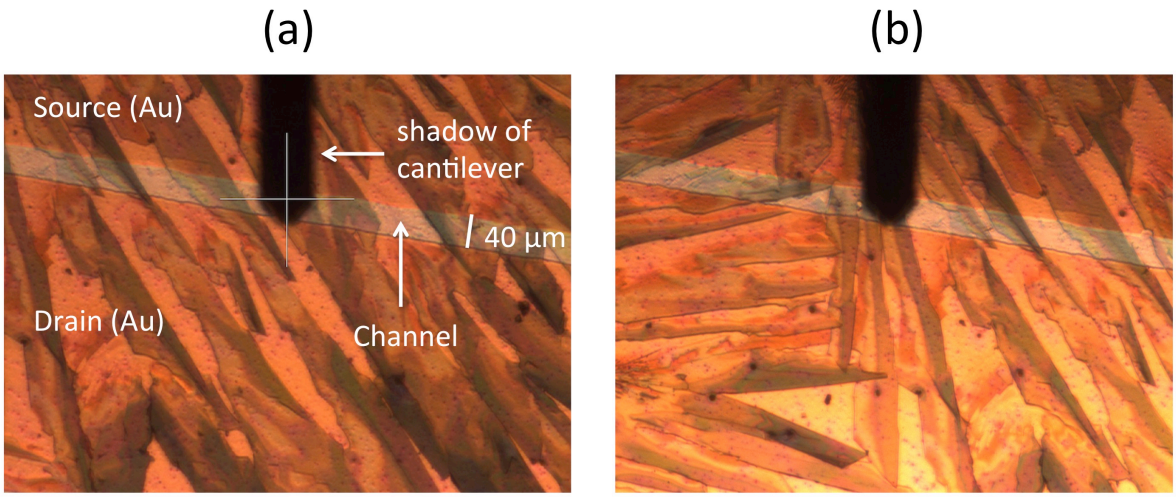

Figure 4.5: Two different areas with different crystallite orientation.

Morphology images, in non-contact mode, of unstrained devices are not easy to take due to the roughness of the surface, for these reasons adaptive scan with slow scan rate is advisable to use.
After making a number of acquisitions to adjust the measurement parameters (see chapter 3.4) we make a 45x45 µm image (that is the maximum image size for this microscope model) that includes all the channel length and both electrodes. Using the Gwyddion software is possible to obtain a 3D rendering to have a more intuitive representation of the surface and height profiles as shown in Figure 4.6. The picture is a more intuitive representation of how semiconductor covered two electrode and how adapted to the topography of the channel. Typically crystals that pass trough the channel and connecting the two electrodes were chosen for our experiments. The height profiles show typical crystal height with range of heights to hundreds nanometers.

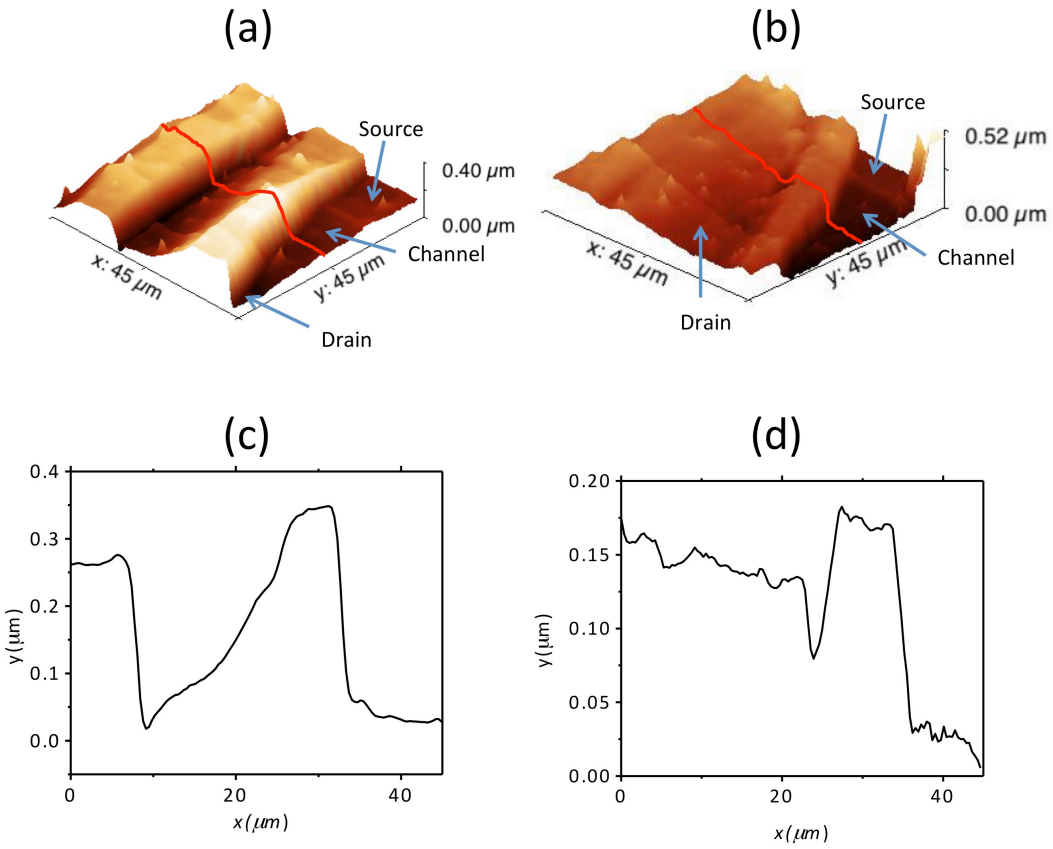

Figure 4.6: (a)-(b) different images take with Park NX10 and processed with Gwyddion software to obtain 3D profile. (c)-(d) plot profile of the two image processed.

Figure 4.7 shows the area selected without applying additional voltages to the transistor. It was chosen deliberately a zone in which there are at same time the semiconductor TIPS-Pentacene, the dielectric and the gold electrode as shown in Figure 4.7 (a).

In these areas the change in potential on the sample surface represents the difference between the work functions of investigated materials. For gold (Au) and aluminium (Al) for example, work function values are available in the literature and equal to 5.1 eV and 4.3 eV.

The graph in Figure 4.7 (c) shows the distribution of values of surface potential in the three selected areas. From this data we note that the difference between work functions of gold and aluminium (the surface potential on the dielectric corresponds to the underlying aluminium gate electrode), corresponds quite well to the difference between the median value of the relative distribution. Hence we can deduce a possible value semiconductor (Pentacene) work function of about 0.25 eV greater than the gold work function.

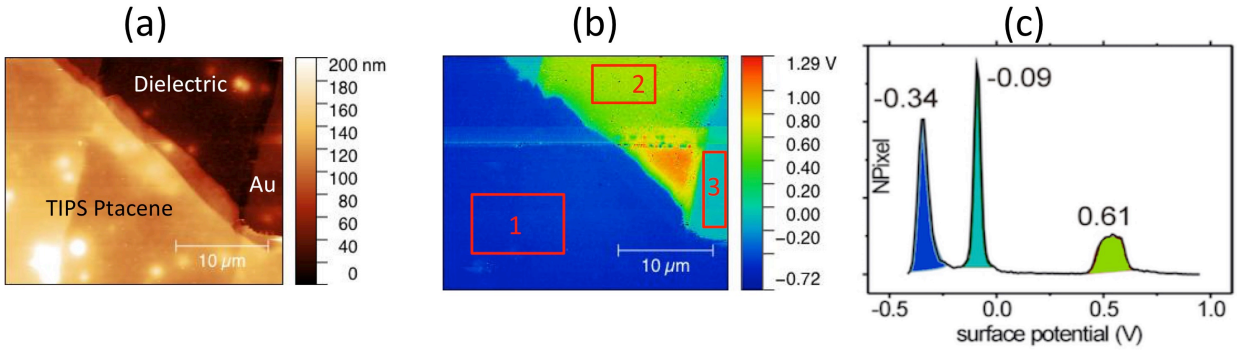

Figure 4.7: (a) The morphological image shows a portion of channel without the semiconductor layer and a portion covered by TIPS Pentacene. (b) KPFM image without potential applied. (c) distribution of the number of pixel shows the three different potential from different materials. The surface potential on the dielectric corresponds to the underlying Aluminum gate electrode.

Another measure that has been made is the surface potential when the transistor is in the saturation regime, then V_D=-5V and V_G=-3V was apply to get this type of condition.

As we can see from the potential map Figure 4.8 (b), the potential decreases homogeneously trough the crystal, this means that there aren't local barrier for charge transport due to crystal defects. The potential profile describes the evolution of potential trough the crystal (Figure 4.8 (c)). Describe in more detail the observations here.

As we know, the charge induced by applying a voltage V_G to the gate in an elemental strip of width dx at distance x from the source above the threshold is:

$$dq = -C_i[V_G - V_T - V(x)]Wdx \tag{4.3}$$

Where W = 23.12 mm and C_i=12nF/cm^2.

Then the current I_D that flows between source and drain is:

$$I_D = \frac{dq}{dt} = \frac{dq}{dx}\frac{dx}{dt} \tag{4.4}$$

So:

$$I_D = WC_i\mu[V_G - V_T - V(x)]dV \tag{4.5}$$

By integrating from source (x'=0,V(x)=0) to drain (x'=x, V(x')=V_D):

$$\int_0^x I_D\,dx = \int_0^{V(x)} WC_i\mu[V_G - V_T - V(x)]dV \tag{4.6}$$

We obtain

$$V(x) = (V_G - V_T) + \sqrt{\frac{2I_D x}{WC_i} - (V_G - V_T)^2} \tag{4.7}$$

In our case, we are in saturation regime ($V_D > |V_G - V_T|$) then we use equation (1.14) for I_D expressions and we obtain the V(x) expression trough the crystal:

$$V(x) = (V_G - V_T) + \sqrt{\frac{1}{L}(V_G - V_T)^2 x - (V_G - V_T)^2} \quad \textbf{(4.8)}$$

This trend of V(x) like $\sqrt{x}$ was experimentally verified from the fit of potential profile into the channel (see Figure 4.8 (c)). The difference between the theoretical curve and the experimental curve is due to the contact resistance at the source and drain terminals. The source and drain contacts in organic TFTs are not easily optimized by conventional processes, such as semiconductor doping or metal alloying. Consequently, organic TFT performance typically suffers from large contact resistance. It was estimated by measuring the potential gap $\Delta V \approx 1.5V$ taken from the graph Figure 4.8 (c) and the current that flows trough the crystal of about $I_D \approx 5E\text{-}6A$ and equal to $R = \frac{\Delta V}{I_D} = 300k\Omega$.

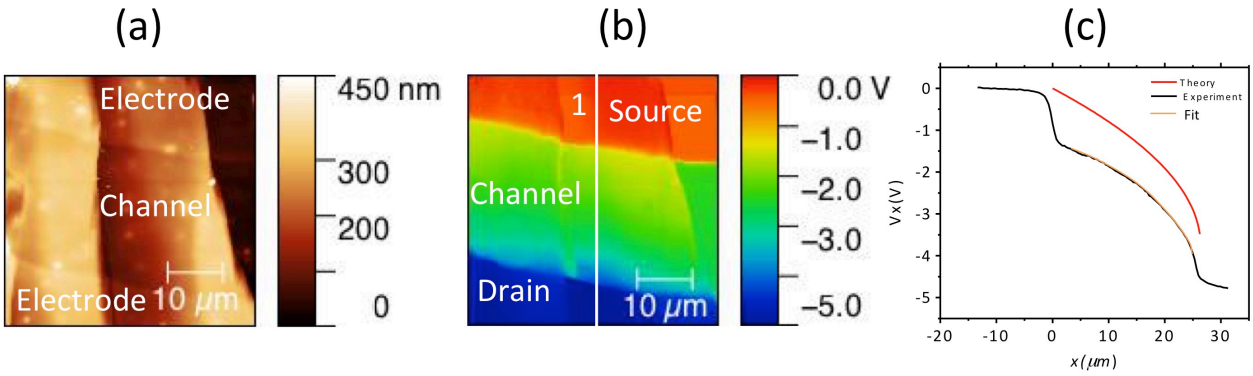

Figure 4.8: (a) The morphological image shows the channel location. (b) KPFM image with potential applied. (c) Potential profile along the crystal.

4.2.2 stressed TIPS-Pentacene TFT i-v characteristic and microscopic analysis

Transfer curves (in our case drain current (I_D) versus gate voltage (V_G) characteristics) of the same devices were recorded for different degrees of strain andin saturation regime (V_D=-5), to study the effect of mechanical strain on charge transport. Transistor characterization was conducted at room temperature in the ambient atmosphere. We find, a decrease in drain current as function of device deformation (Figure 4.9).

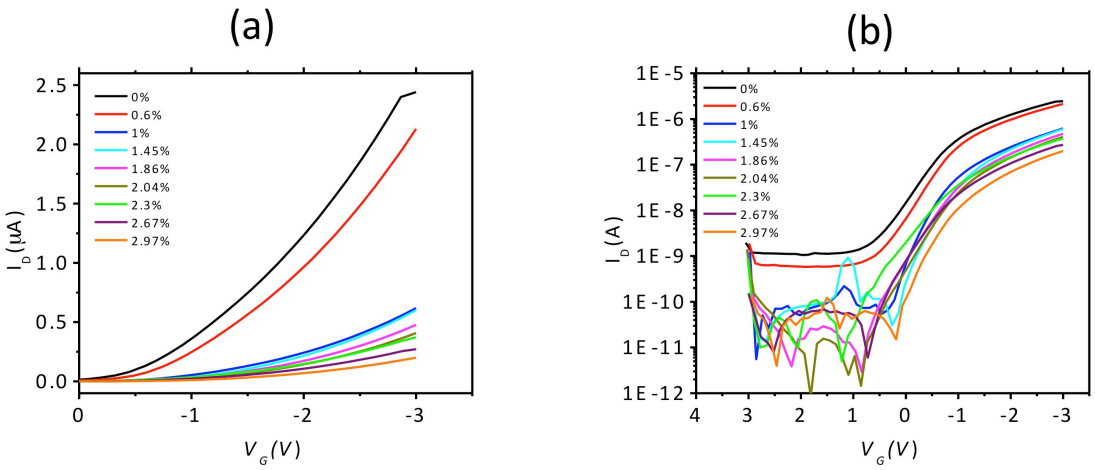

Figure 4.9: Electrical characteristic of a TIPS Pentacene TFT device. (a) transfer curve recording during successive device bending with V_D=-5. (b) same transfer curve with a different scale (Log10).

Experiments were performed in the dark. The mobilities were relatively insensitive to light, although transistor off-currents tended to increase with the ambient light intensity.

From the transfert curves I calculated the mobility μ, the threshold voltage V_{TH} and the off current I_{OFF} (Figure 4.10).

Results plotted in Figure 4.10 (a) show a distinctive behaviour in which specific strain intervals can be defined: μ show large discontinuos change at specific strain values which permit to define four intervals as indicated in the figure. Within the intervals, transport parameters vary only gradually or even remain constant, whereas at the borders large variations are observed. That allows us to suppose that after a certain degree of deformation an irreversible process occurred in the device structure (in the active layer), that causes an abrupt lowering of μ. Instead within the intervalls the active layer absorbs the induced mechanical strain until a new critical value is reached an more severe changes occur, reducing further μ again.

A similar trend is shown in Figure 4.10 (b), where off currents I_{OFF} were plotted versus strain. Experimental points with $\varepsilon > 2.3\%$ manifest an increasing off current, probably due to the fact that at high degree of mechanical strain, the formation of areas in which charge carriers may be trapped sets-in. This phenomenon does not occur for the mobility μ because in this kind of device that works in accumulation mode, the charge transport is an interface phenomenon (charge were induced at the dielectric interface, applying the V_G potential) and only changes in this thin region (tick some atomic layers) cause change in mobility rate, while the off-current includes the whole crystal, and changes in any point in the crystal cause changes in I_{OFF}.

The threshold voltage V_{TH} remains almost constant with a slight drift towards negative values.

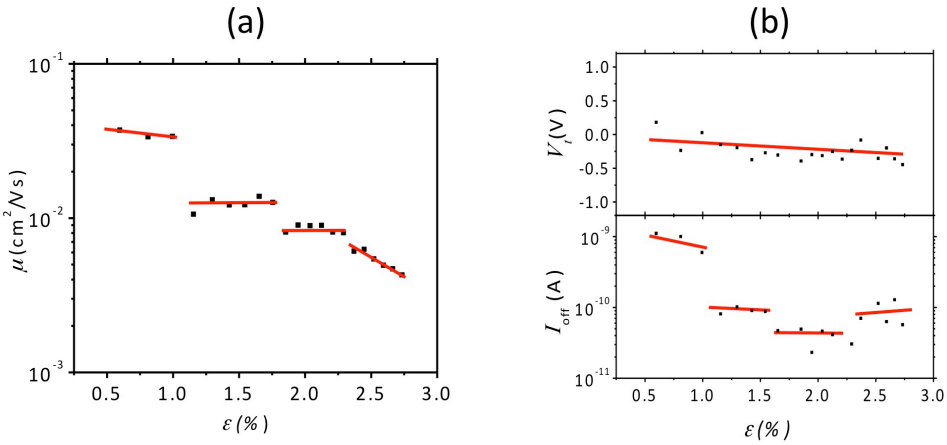

Figure 4.10: (a) mobility μ versus strain%. With arrow different strain step have been indicated. (b) Threshold voltage V_T and off current I_{OFF} versus strain%.

To investigate this distinctive behaviour in electrical characteristics we performed contemporaneously morphological and electrical investigation of the deformed device. KPFM was used to obtain surface potential maps containing the active layer and the electrodes on the same device in parallel to electrical characterizations. In all measurements the transistor was kept at constant grain and gate bias of V_D=-5V and V_G=-3V to drive the saturation current through the semiconducting microcrystals.

To investigate the nanoscale morphological changes of the substrate structure produced by strain, we obtain morphological images 45μm x 45μm with different degree of mechanical strain, in this case from 0.6% to 3%. For the purpose of the research, an area with crystals that connect the two gold electrodes crossing the TFT channel was chosen. In particular the same area for different degree of mechanical strain was investigated to observe the behaviour of crystals, under increasing levels of mechanical deformation. Morphological images (Figure 4.11) show that small strain did not cause any noticeable variation in the structure of the active layer. Instead the surface potential maps so severe changes caused by strain. KPFM images shows more clearly that the actual cracks formation causes potential drops (Figure 4.12). Cracks can be easily detected in the regions where surface potential shows a sudden change in value, which is reflected in a change in colour in these KPFM images. In fact in correspondence of these change in potential in KPFM images, AFM image shows the presence of a crack in the crystal.

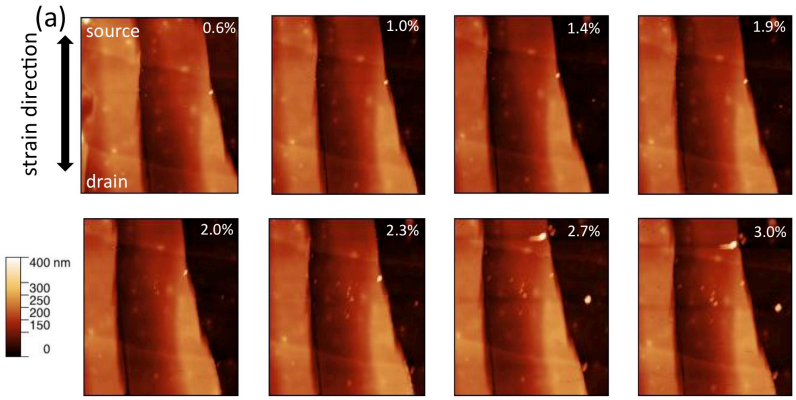

Figure 4.11: Morphological images in non contact mode image taken with NX10 at different strain.

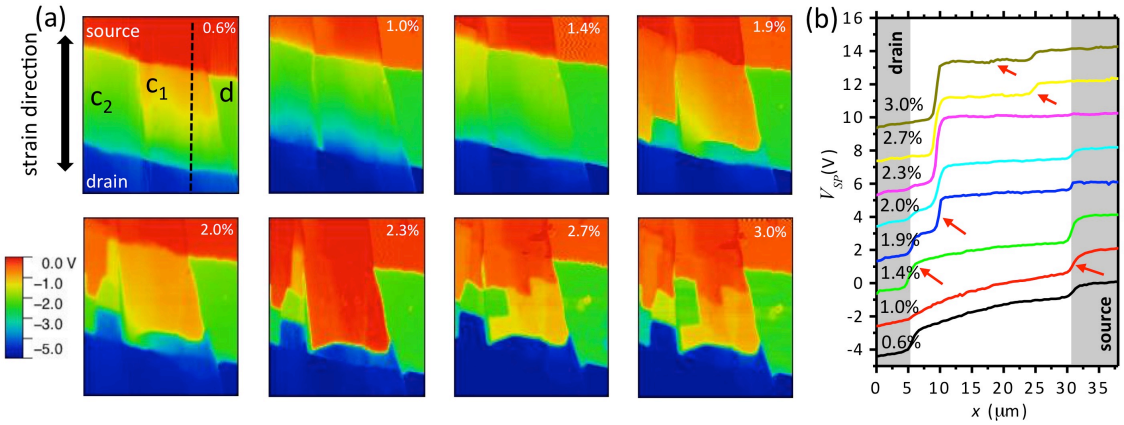

Figure 4.12: (a) KPFM images taken with increasing strain. (b) potential profile taken across the channel shows voltage drops in correspondence of the cracks formation.

The drops in mobility and off current in the graphs shows in Figure 4.10 can be explained considering that the cause of these particular trends is due to a formation of cracks in the crystal of the active layer. Crack generation is the irreversible process occurred in the active layer of the device that causes lowering of μ and I_{OFF}. Being crystal not elastic, only cracks can absorb mechanical strain for a while, but increasing strain will lead to new crack formation. This cracks generation, which includes all crystals in the active layer, changing the mobility and off current as shown in Figure 4.10.

The formation of new cracks was investigated more detailed in this experimental work, as shown in KPFM images (Figure 4.12).

In saturation regime the surface potential V_{SP} follows essentially the electrostatic potential in the accumulation layer in the semiconductor thus allowing to draw conclusion on local carrier concentration and variation in resistance. Figure 4.12 shows the resulting maps of V_{SP} at different characteristic strain values. Source and drain electrode can easily be distinguished in these plots as

they appear as isopotential surfaces at the values imposed by the source measure unit (V_S=0 V, V_D=-5V) plus an offset due to the contact potential difference to the AFM tip.

Observing the AFM image of the same region (Figure 4.11), it is possible to notice that part of the channel region is not covered by organic semiconductor. In these areas (see d in Figure 4.12 (a)) the V_{SP} is constant and not affected by strain.

Areas covered by organic crystals (c_1 and c_2 areas in Figure 4.12) shows a complex behavior and increasing the mechanical strain, new cracks were formed and cause change in surface potential (whit formation of local barriers that increased resistance of the semiconductor) as shown in the profile taken in the same position for different degree of strain (Figure 4.12 (b)).

At low strain values, steps in V_{SP} are present only at the contacts between electrodes and semiconductor. Along the channel V_{SP} decrease gradually, until arriving to a maximum value ear the drain electrode, due to the formation of the pinch-off area. At certain strain cracks appear first at the electrode contacts. Increasing the strain new cracks that reflects potential barrier in KPFM images appear also away from the electrodes. Cracks are mostly orthogonal to the strain direction. Discontinuities in parallel direction are due to the borders between microcrystals. At large strain value it is observed a formation of independent patches with constant V_{SP}. Some of these patches in KPFM image seem to be electrically isolated as they exhibit a V_{SP} value similar to areas not covered by semiconductor.

To confirm this crack formation mechanism, another region with a different crystal orientation was investigated as shown in Figure 4.13. This result shows more clearly how the formation of new cracks changes the potential profile of the crystal.

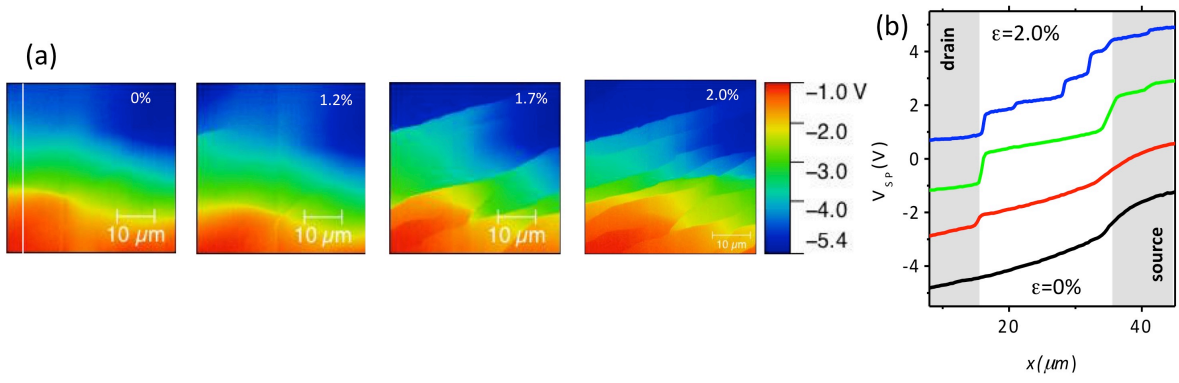

Figure 4.13: (a) KPFM images taken with increasing strain in a different area of the active layer. (b) potential profile shows more clearly voltage drops in correspondence of the cracks formation.

To get a complete qualitative description of a crack generation and evolution, I get morphological image 2 μm x 2 μm in correspondence of an evident potential downshift at a resolution of 256 pixels each scanned line and at same time KPFM images was taken for two different strain, respectively 1.55% and 1.86% (Figure 4.14).

Difference in crack depth and potential profile were noted, at the greater strain, the crack depth was increased, as shows in Figure 4.14 (f), but the gap in potential was less than the change in potential with smaller strain. This effect is due by the fact that at greater mechanical device deformation, crack formation was increased, then the current that flow decreased and the results is that potential drops in the single crack I measured was less than the case when smaller strain was applied.

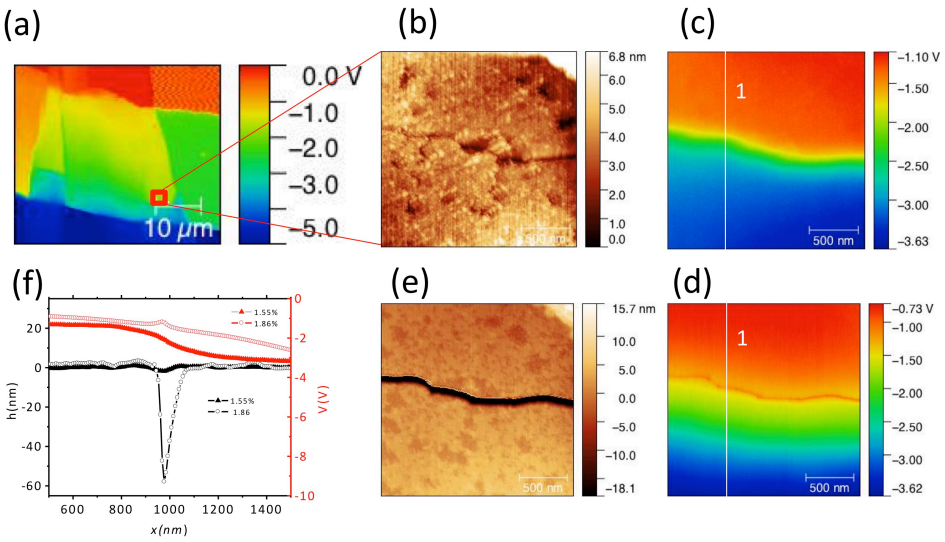

Figure 4.14: (a) KPFM image show the area were zoomed image (2µm x 2µm) was taken. (b)-(c) morphological and surface potential images with strain 1.55%. (d)-(e) morphological and surface potential images with strain 1.86%. (f) comparison between morphological and potential profile of the same crack at different strain.

Another region with a different crystal orientation was investigated. As shown in Figure 4.15, the comparison between the same area at different strain (1.16% and 1.8% respectively) shows more clearly the same behavior, confirming what previously said.

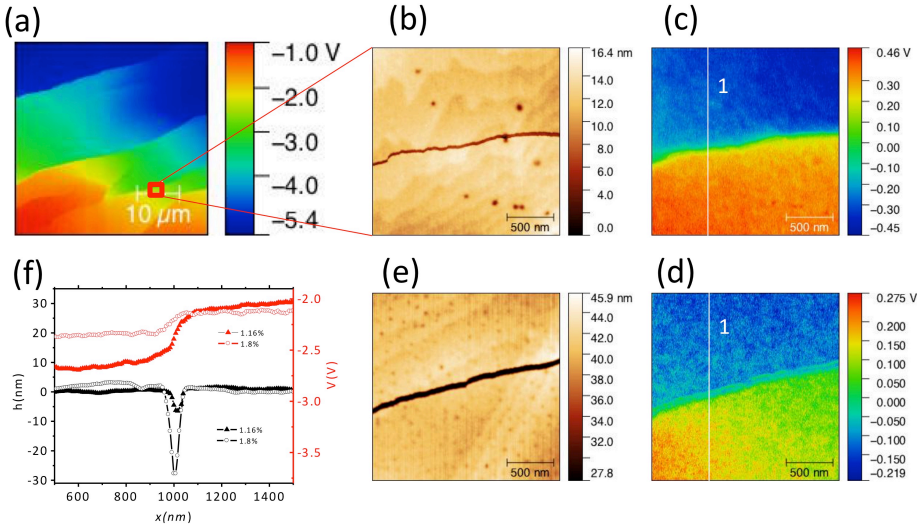

Figure 4.15: (a) KPFM image show the area were zoomed image (2µm x 2µm) was taken. (b)-(c) morphological and surface potential images with strain 1.16%. (d)-(e) morphological and surface potential images with strain 1.8%. (f) comparison between morphological and potential profile of the same crack at different strain.

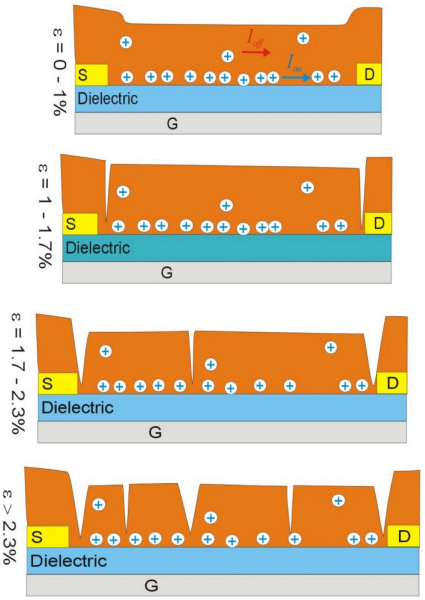

Figure 4.16: model of micro-crack generation. From top to bottom strain was increased and crack were formed.

Combining the microscopic findings with the evolution of transistor performance I arrive at the following mechanism of transistor degradation under strain: at low strain values ($\varepsilon < 1\%$) the microcrystal resists the mechanical deformation; transistor performance starts to deteriorate only gradually probably due to reduced charge injection and extraction at electrodes under strain. Finally the micro-crystals break at the contacts and a large drop in transistor current is observed. I distinguish bulk transport, as responsible for the relatively high-off current, from interfacial transport in the accumulation layer. The latter happens at the buried interface to the elastic gate dielectric. I hypothesize that this distributes the mechanical stress more evenly over the microcrystal and reduces crack opening thus maintaining transport properties albeit with reduced efficiency. Instead transport through the bulk of the crystal is effected much stronger by cracks, causing an order of magnitude drop in off-current which exceeds the reduction in mobility. Beyond the drop at $\varepsilon = 1\%$ transistor performance remains relatively stable as existing cracks absorb the deformation until at $\varepsilon = 1.9\%$ new crack formation sets in and causing a disruptive change in transport properties. Again the new crack is able to absorb deformation and to stabilize the strain response until at $\varepsilon > 2.3$ more complex fractures of the microcrystal start to happen. The complexity and the directionality of the multitude of crystal fractures which appear in this regime is determined by details of the shape of each individual microcrystal. Due to the varying thickness of microcrystals, dislocations and then cracks appear also in the directions not orthogonal to the applied strain. At this stage cracks interrupt electrical transport severely and independent patches with constant surface potential emerge. These isolated patches are also associated to the observed increase in off-current: Due to the very weak electrical connection,

charging and decharging processes of these patches are very slow and during the fast transfer-sweep they act as charge carrier reservoirs contributing to a measurable drain current also in the off-state of the transistor.

4.3 P3HT

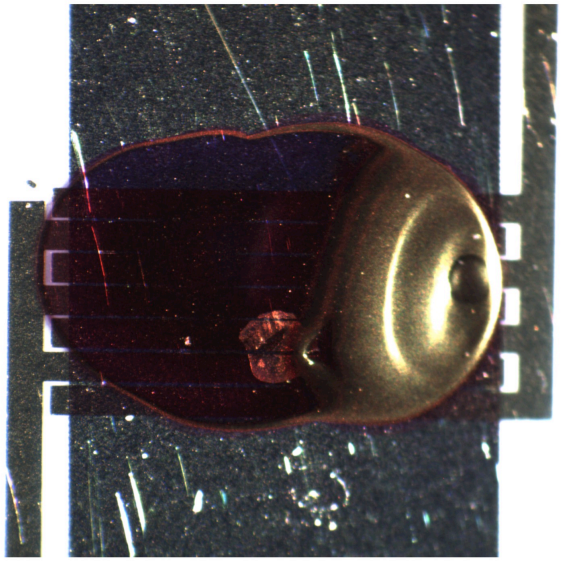

Figure 4.17: Image taken with the optical microscope showing the P3HT after the deposition process. Under the semiconductor layer is possible to see the interdigized electrode.

The sample analysed (Figure 4.17) is an OFET realized with an organic semiconductor as active layer called P3HT, that is one of the most popular [23] and performing organic molecule characterized by its good electronic properties, solubility, and stability, such as Pentacene, is used primarily in organic thin-film transistors (OTFT).

In the experiment the sample was bend to exert strain on the active layer while transfer characteristic were acquired to determine macroscopic transport properties and SKPM was used to delineate the morphology and the surface potential of the P3HT film under strain. Transfer curves (in our case drain current (I_D) versus gate voltage (V_G) characteristics) of the same devices were recorded for different degrees of strain at V_D=-5, to study the effect of mechanical strain on charge transport. Transistor characterization was conducted at room temperature in the ambient atmosphere. Experiments were performed in the dark. The mobilities were relatively insensitive to light, although transistor off-currents tended to increase with the ambient light intensity [25].

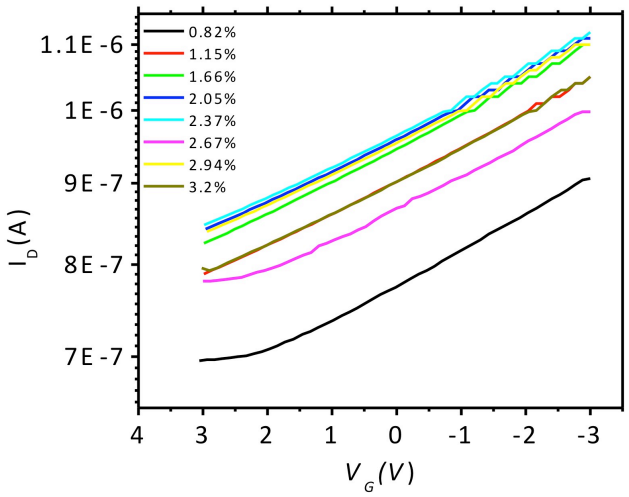

Figure 4.18: Electrical characteristic of a P3HT TFT device. (a) Transfer curve recording during successive device bending with V_D=-5.

No significant changes in drain current as function of device deformation (Figure 4.18) were found. I note that transfer curves show that the device never turns off in the 3 V ÷ -3 V range. As an explanation I suggest that the active layer reacts to light and oxidation both causing doping of the semiconductor [24].

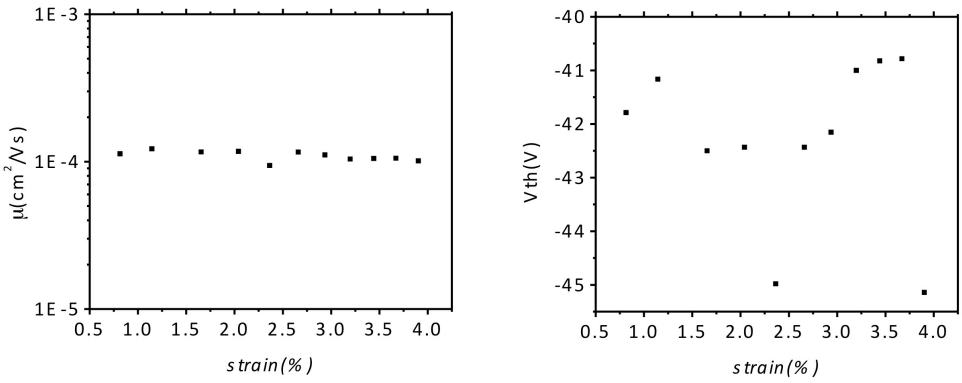

Figure 4.19: (a) mobility μ versus strain%. (b) Threshold voltage V_T and off current.

From the transfer characteristics the values of mobility μ, and threshold voltage V_{TH} were extracted (see Figure 4.19). No significant difference in μ, and V_{TH} as a function of strain were found.

After these measurements, I focus in the analysis on the microscopy of particular areas in order to investigate morphological or surface potential changes when a mechanical strain is applied.

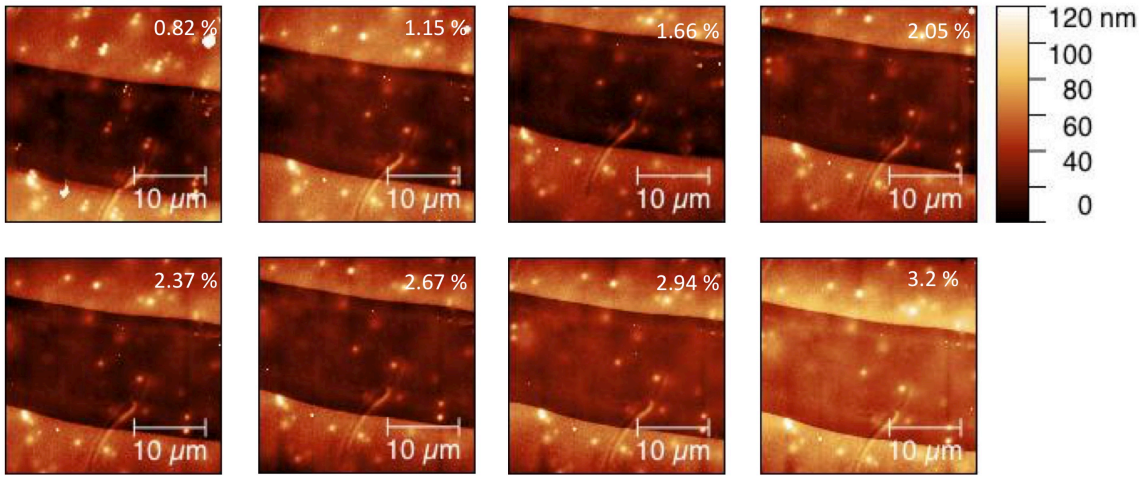

Figure 4.20: Morphological images in non contact mode image taken with NX10 at different strain.

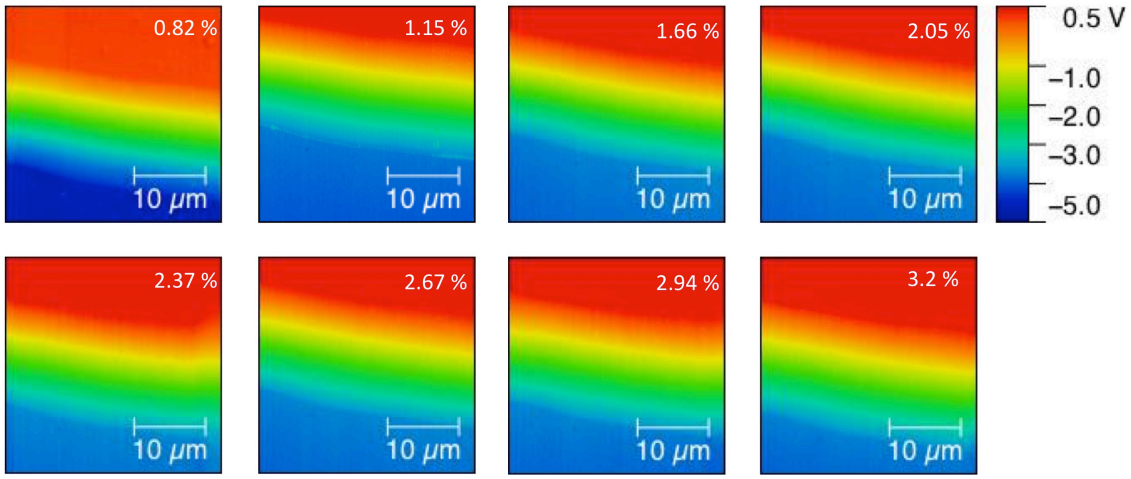

Figure 4.21: Potential profile images taken with NX10 at different strain.

Morphological images (Figure 4.20) show that strain did not cause any noticeable variation in active layer morphology. KPFM images in Figure 4.21 show the same behaviour. Unlike TIPS-Pentacene, no abrupt changes in surface potential are notable instead the gradual variation across the channel is not affected by strain. Hence both, morphology as well as surface potential images confirm that no significant change occurs in the active layer. In particular the same area for different degrees of mechanical strain was investigated to observe the behaviour the active layer, under increasing mechanical deformation.

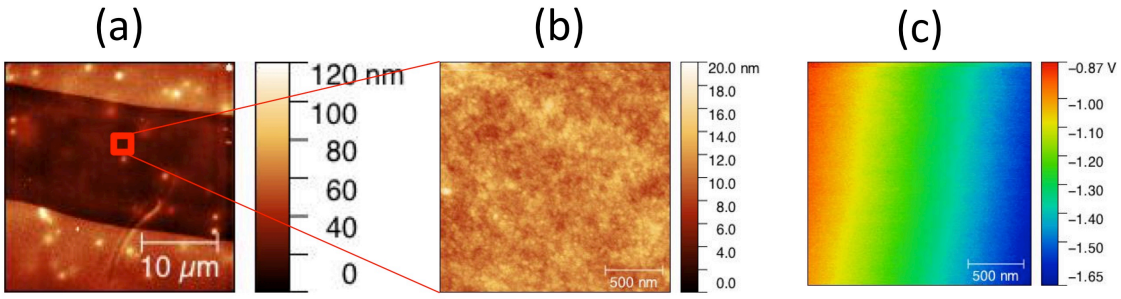

Figure 4.22: (a) morphological P3HT active layer image, (b)-(c) zoomed area and relative surface potential.

As we can see in Figure 4.22, the zoomed area shows that the thin film taken into consideration is homogenous albeit with rather high roughness (~10 nm) for a spin cast film. No special preferential direction of growth or other features indicating crystallinity are observable, in agreement with the pronounced amorphous structure of the polymer film. Thus charge transport can be assumed to be isotropic [24]. This is further confirmed by map of surface potential, which does not show any significant structure or other correlation to the morphology image.

Thus I conclude that P3HT behaves very differently from TIPS-Pentacene crystals. Due to the amorphous structure of the polymer film an elastic behaviour also at higher strain values remains and no crack formation or other rupture processes occur. Interestingly the elastic deformation does not have an impact on charge transport. This could be explained by the strong impact of local disorder and trap states on transport in this polymer. The small strain values does not notably change the related microstructure in the polymer.

5 Conclusion and Outlook

In this thesis I established an Atomic Force Microscopy (AFM) technique to investigate at the nanoscale the effects of mechanical deformation on flexible thin film transistors (TFT). The technique exploits non-contact interaction between the AFM probe and the transistor surface to minimize interaction forces with the deformed, free-standing sample and to reduce tip wear. Topographic imaging is combined with Scanning Kelvin Probe Microscopy (SKPM) to obtain a map of the surface potential of the biased thin film transistor. For a semiconducting film operated in accumulation due to field effect, the surface potential is directly related to the electrostatic potential in the accumulation layer. Thus it provides information on charge carrier density and local electric field in the semiconducting channel, both crucial measures to detect local variations in the transport properties of the semiconductor as possibly caused by mechanical strain.

As test cases with relevance for flexible organic electronics I studied the strain response of two different organic semiconducting thin films: First a microcrystalline thin film of the small molecule organic semiconductor TIPS-pentacene, a reference material for printed p-type organic TFTS. Second P3HT, a reference material for polymeric semiconductors. In both cases the organic thin film was deposited on TFT test structures fabricated on flexible PEN substrates. Mechanical deformation was induced by a specially designed sample holder mounted under the AFM head and connected electrically to measure contemporaneously macroscopic transistor characteristics. A quantitative model was developed to determine the resulting strain exerted on the active layer as a function of deformation. Due to the large thickness of the substrate, strain in the active layer results essentially from a stretching deformation and is varied in the experiments between 0% and 3%.

The findings show very distinct behaviours of the two organic semiconductors: TIPS pentacene based organic TFTs are very sensitive to strain and a reduction of transport properties is observed. The degradation was found to happen abruptly in distinctive steps. The microscopic analysis clearly demonstrates that the formation of nano-cracks is at the origin of the device degradation. A detailed analysis of the macroscopic electrical characterization and the microscopic images allowed to derive a model of microcrystal rupture in which at critical strain values cracks are formed which can absorb further stretching deformation thus stabilizing the strain response of the device for a defined interval until new crack formation sets in. In contrast P3HT remains unaffected by strain and the microscopic images reveal no features but isotropic topography and surface potential distribution. These findings are explained by the amorphous structure of the polymer film which permits an elastic response even at higher strain values.

6 Bibliography

[1] P. Cosseddu, G. Tiddia, S. Milita, and a. Bonfiglio, "Continuous tuning of the mechanical sensitivity of Pentacene OTFTs on flexible substrates: From strain sensors to deformable transistors," *Org. Electron. physics, Mater. Appl.*, vol. 14, no. 1, pp. 206–211, 2013.

[2] I. M. Graz and S. P. Lacour, "Flexible pentacene organic thin film transistor circuits fabricated directly onto elastic silicone membranes," *Appl. Phys. Lett.*, vol. 95, no. 24, pp. 93–96, 2009.

[3] V. Scenev, P. Cosseddu, a. Bonfiglio, I. Salzmann, N. Severin, M. Oehzelt, N. Koch, and J. P. Rabe, "Origin of mechanical strain sensitivity of pentacene thin-film transistors," *Org. Electron. physics, Mater. Appl.*, vol. 14, no. 5, pp. 1323–1329, 2013.

[4] I. Kymissis, *Organic Field Effect Transistors*. 2003.

[5] W. Brütting, *Physics of orgnic semiconductors*, Wiley-VHC. 2005.

[6] T. N. Prize, "The Nobel Prize in Chemistry , 2000 : Conductive polymers," pp. 1–16, 2000.

[7] S. Savagatrup, A. D. Printz, T. F. O'Connor, A. V. Zaretski, and D. J. Lipomi, "Molecularly stretchable electronics," *Chem. Mater.*, vol. 26, no. 10, pp. 3028–3041, 2014.

[8] "Realisation and Characterisation of Organic Electronic Devices for E – textiles applications," no. March, 2011.

[9] and H. Petrucci, Harwood, *Chimica Generale, Principi e moderne applicazioni*. 2002.

[10] B. G. Johansson, "No Title," *Scand. J. Clin. Lab. Inv.*, vol. 29(124), pp. 7–19., 1972.

[11] G. Horowitz, "Interfaces in Organic Field-Effect Transistors," *Adv. Polym. Sci.*, no. june 2009, pp. 1–34, 2009.

[12] N. K. Dr., *Organic Electronic Devices and Their Functional Interfaces*. 2007.

[13] M. Nonnenmacher, M. P. O. Boyle, H. K. Wickramasinghe, and M. Nonnenmacher, "Kelvin probe force microscopy Kelvin probe force microscopy," vol. 2921, no. 1991, 2016.

[14] H. Hoppe, T. Glatzel, M. Niggemann, A. Hinsch, and M. C. Lux-steiner, "Kelvin Probe Force Microscopy Study on Conjugated Polymer / Fullerene Bulk Heterojunction Organic Solar Cells," 2005.

[15] X. J. Raj and T. Nishimura, "Investigation of the Surface Potential on Iron Nanoparticles During the Corrosion by Atomic Force Microscopy (AFM) and Kelvin Probe Force Microscopy (KFM)," vol. 9, pp. 2090–2100, 2014.

[16] N. G. Clack, K. Salaita, and J. T. Groves, "Electrostatic readout of DNA microarrays with charged microspheres," vol. 26, no. 7, pp. 825–830, 2008.

[17] E. Finot, Y. Leonenko, B. Moores, L. Eng, M. Amrein, and Z. Leonenko, "Effect of Cholesterol on Electrostatics in Lipid - Protein Films of a Pulmonary Surfactant," vol. 26, no. 13, pp. 1929–1935, 2010.

[18] P. S. Corporation, *NX10 user's manual*. 2013.

[19] V. L. Mironov, *Foundamentals of Scanning Probe Microscopy*. 2004.

[20] P. Grag Haugstad, Eaton, Peter, West, *Atomic Force Microscopy*. 2010.

[21] P. S. Corporation., *XEP Data acquisition Program for XE series SPM*. 2011.

[22] P. Klapetek and N. and C. Anderson, *Gwyddion user guide*. .

[23] L. Bürgi, T. Richards, M. Chiesa, R. H. Friend, and H. Sirringhaus, "A microscopic view of charge transport in polymer transistors," *Synth. Met.*, vol. 146, no. 3, pp. 297–309, 2004.

[24] C. Poelking, K. Daoulas, A. Troisi, and D. Andrienko, "Morphology and Charge Transport in P3HT : A Theorist ' s Perspective," 2014.

[25] A. Chortos, J. Lim, J. W. F. To, M. Vosgueritchian, T. J. Dusseault, T. H. Kim, S. Hwang, and Z. Bao, "Highly stretchable transistors using a microcracked organic semiconductor," *Adv. Mater.*, vol. 26, no. 25, pp. 4253–4259, 2014.